THE ASTROPHYSICAL JOURNAL, 319:575–600, 1987 August 15

ANGULAR MOMENTUM FROM TIDAL TORQUES

JOSHUA BARNES
Institute for Advanced Study

AND

GEORGE EFSTATHIOU
Institute of Astronomy, Cambridge, England
Received 1986 August 25; accepted 1987 February 9

ABSTRACT

We describe results for the origin of angular momentum of bound objects in large cosmological N-body simulations. Three sets of models are analyzed: one with white-noise initial conditions and two in which the initial conditions have more power on large scales, as predicted in models with cold dark matter (CDM).

We study the growth and distribution of angular momentum in individual objects. The specific angular momentum distribution of bound clumps increases nearly linearly with radius, but the orientation of the angular momentum in the inner high-density regions is often poorly correlated with that of the outer parts. The angular momentum of proto-objects grows as the first power of time while their overdensity is less than unity, in agreement with linear perturbation theory. Objects with pronounced substructure couple more effectively to the tidal field and so acquire more angular momentum. However, the nonlinear evolution of substructure in the inner regions of groups transports angular momentum to their outer parts. The final angular momentum of nonlinear clumps may be substantially lower than the angular momentum acquired during the linear growth phase. These nonlinear effects may play a key role in determining the Hubble sequence.

Statistical analysis of large catalogs of objects shows that the dimensionless spin parameter λ is remarkably insensitive to the initial perturbation spectrum and has a median value $\lambda_{\rm me} \sim 0.05$. Thus the generation of angular momentum in hierarchical clustering models is not critically dependent on the specific shape of the primeval spectrum. The quantity λ is weakly correlated with mass and internal substructure and is uncorrelated with initial overdensity. In CDM models, groups with high λ-values tend to have nearer neighbors and are *more* strongly clustered than groups with low λ; these effects are weaker or absent in white-noise models. There is little or no significant correlation between spin orientations of nearest neighbor clumps in either class of model.

Subject headings: galaxies: clustering — galaxies: formation — galaxies: internal motions

I. INTRODUCTION

If galaxies and clusters formed by gravitational instability of small density perturbations, they will have acquired angular momentum through tidal interactions with their neighbors (Hoyle 1949; Peebles 1969). Analytic descriptions of this process have proved to be difficult, even in linear perturbation theory, and almost totally inadequate in modeling the nonlinear phase of structure formation.

Peebles (1969) used linear theory to estimate the angular momentum growth in randomly placed spherical regions, assuming that the power spectrum of the density fluctuations was of the form

$$|\delta_k|^2 \propto k^n \, . \tag{1}$$

He matched the results with those of a simple nonlinear model in which the torque on a protosystem was calculated as the product of its quandrupole moment with the tidal field of neighboring point masses. Peebles's calculation suggested that the dimensionless spin parameter,

$$\lambda \equiv J|E|^{1/2}G^{-1}M^{-5/2} \, , \tag{2}$$

of a typical bound system should be roughly $\lambda \approx 0.08$. (Here J, E, and M are, respectively, the total angular momentum, energy, and mass of the system; G is the gravitational constant.) This calculation can be considered only as a rough guide to the correct answer. For example, the linear part of the calculation diverges for spectral indices outside the range $-1 < n < 0$ because of spurious coupling between short- and long-wavelength modes. The linear growth rate of J is inapplicable to the early stages of protogalaxy evolution because Peebles calculates J for spherical regions, so the angular momentum grows only to second order in perturbation theory. A different analysis has been given by Doroshkevich (1970) and expanded by White (1984). These authors show that the angular momentum of a Lagrangian volume encompassing the material which eventually ends up in a bound grows to first order. However, the magnitude of J is uncertain in the latter approach, since it is difficult to designate the boundary of a protogalaxy analytically.

Zel'dovich and Novikov (1983) recognized that detailed predictions from the tidal torque model would probably require cosmological N-body simulations. This is the approach adopted in this paper. Our work is an extension of previous numerical studies which dealt mainly with white-noise ($n = 0$) initial conditions with $\Omega = 1$. Efstathiou and Jones ran 1000 particle N-body simulations and found that the 90 and 10 percentile points in the distribution of λ for bound clumps correspond to $\lambda = 0.11$ and $\lambda = 0.03$, respectively, with a median $\lambda = 0.06$. This result was confirmed by Efstathiou and Barnes (1983, hereafter EB) using a 20,000 particle simulation. They also found a trend for massive clumps to have lower λ

values than less massive clumps. They ran several 1000 particle models with spectral indices $n = +2$ and $n = -1$ and found evidence that the λ distribution is not sensitive to initial conditions. We have been motivated to reexamine this problem because it is now feasible to run many large-N simulations. We can therefore begin to ask more detailed questions concerning the internal distribution of angular momentum, the nonlinear effects of substructure, correlations with large-scale structure, and so on.

Recent work on galaxy formation and clustering suggests that equation (1) with $n = 0$ may be a poor approximation to the postrecombination fluctuation spectrum. Values of $n \lesssim -1$ are in closer accord with the observed two-galaxy correlation function and the multiplicity function of groups and clusters (Gott, Turner, and Aarseth 1980; Efstathiou and Eastwood 1981). In one of the most attractive models, the mean mass density of the universe is dominated by cold weakly interacting dark matter (CDM; see Blumenthal *et al.* 1984). For constant-curvature primordial fluctuations, the postrecombination power spectrum in this model is well approximated by

$$|\delta_k|^2 \propto \frac{k}{(1 + \alpha k + \beta k^{3/2} + \gamma k^2)^2}, \tag{3}$$

where $\alpha = 1.7l$, $\beta = 9.0l^{3/2}$, $\gamma = 1.0l^2$, and $l \equiv 1(\Omega h^2 \theta^{-2})^{-1}$ Mpc[1] (Davis *et al.* 1985, hereafter DEFW). This spectrum exhibits a gradual transition from the primordial slope $n = +1$ on large scales to $n = -3$ on small scales. DEFW have described an extensive series of N-body simulations designed to study the formation of large-scale structure in this model. They find that $\Omega = 1$ models are acceptable, provided that luminous galaxies formed only at the high peaks in the initial density field ("biased" galaxy formation; see also Bardeen 1986; Kaiser 1986). The density peaks are more highly clustered than the mass, in qualitative agreement with the argument for linear Gaussian density fields given by Kaiser (1984). Hence in biased galaxy formation models, luminous galaxies exaggerate the clustering strength of the mass distribution. An unbiased low-density universe with $\Omega_0 = 0.2$ was found to give a somewhat less satisfactory match to observations of galaxy clustering. CDM universes with $\Omega_0 h^{-4/3} < 0.2$ are also incompatible with upper limits on the fine-scale anisotropy of the microwave background radiation (Bond and Efstathiou 1984). In Davis *et al.*'s specific example of biasing, the value of the Hubble parameter is $h \approx 0.5$, and the effective spectral index on scales relevant to galaxy formation is roughly $n = -2.4$.

These results must be regarded as preliminary at this stage. No successful mechanism for biased galaxy formation has yet been demonstrated (but see Rees 1985; Silk 1985; Dekel and Silk 1985; Frenk *et al.* 1987 for various ideas), and the observational constraints on the model are still relatively weak. Nevertheless, the hypothesis that galaxies formed at the high peaks in a universe dominated by CDM has excited considerable discussion and speculation, some of which may remain relevant even if the specific details of the CDM picture are incorrect. For example, Blumenthal *et al.* (1984) suggest that galaxies forming around the highest peaks ($\gtrsim 3\sigma_g$, where σ_g is the rms density fluctuation on a galactic scale) acquire less angular momentum via tidal torques and therefore become ellipticals, while lower peaks ($1\sigma_g$–$2\sigma_g$) spin more rapidly and become disk galaxies. Since high peaks are statistically concentrated toward the future sites of rich clusters (see Bardeen *et al.* 1986), Blumenthal *et al.* predict a relationship between the morphology of galaxies and their environment in qualitative agreement with observations by Dressler (1980). Hoffmann (1986) has presented a simplified calculation indicating that the required anticorrelation between angular momentum and initial overdensity arises naturally in hierarchical clustering models. We are skeptical of such claims. First, it seems unnatural that the angular momentum of a proto-object, which depends on its shape and the local tidal field, should be closely related to a *global* threshold. Second, the angular momentum of a nonlinear clump is unlikely to be accurately predicted by linear theory. Angular momentum growth is abruptly truncated once a cluster reaches an overdensity on the order of unity, and may decrease substantially thereafter if it is inhomogeneous and nonaxisymmetric, as first pointed out by Frenk *et al.* (1985). Third, one generally requires a knowledge of the *joint* distribution of several variables, e.g. J, E, and M, to apply even the simplest arguments regarding the final state of collapsed protogalaxies (Fall and Efstathiou 1980).

Thus, one of our main aims in this paper is to examine the generation of angular momentum in simulations with "more power on large scales," such as CDM models (eq. [3]), and to compare the results with simulations run with white-noise initial conditions. Numerical results for the special case $n = 0$ have figured prominently in many discussions of galaxy formation (e.g., Fall and Efstathiou 1980; Silk and Norman 1981; Gunn 1982; Faber 1982). It is clearly important to check whether results derived from white-noise models are applicable to a wider range of spectral indices. We do not concentrate on simulating the exact initial conditions appropriate to galactic scales in the CDM picture because this poses difficult (although not insurmountable) numerical problems. In our view, such specific modeling does not seem warranted at this stage. For example, recent work by White *et al.* (1987) suggests that the biased CDM model proposed by DEFW does not account for the strong clustering of Abell clusters (Bahcall and Soneira 1983) and does not lead to large-scale velocity fields such as those reported by Collins, Joseph, and Robertson (1986) and Burstein *et al.* (1986). Our models have substantial power on large scales and should be adequate to test whether any features of the tidal torque picture are *unduly* sensitive to the spectral shape.

The N-body simulations and the algorithm used to identify groups are described in § II. In § III we give examples of individual objects and study their dynamical properties. Section IV presents an investigation of correlations between λ and various other parameters (e.g., group mass, presence of substructure, degree of clustering); we also describe the evolution of angular momentum and test for correlations between the spin directions of group pairs. Our main conclusions are summarized in § V.

II. NUMERICAL SIMULATIONS AND GROUP CATALOGS

a) Numerical Simulations

The N-body simulations that we analyze here were run using the high-resolution cosmological P3M (particle-particle particle-mesh) code described by Efstathiou and Eastwood (1981) and Efstathiou *et al.* (1985). This code can follow the motion of a large number of particles (typically $N = 32768$) within a periodic computational cube of length L. The gravita-

[1] Here h is the Hubble constant in units of 100 km s^{-1} Mpc^{-1}, and θ is the microwave background temperature in units of 2.7 K.

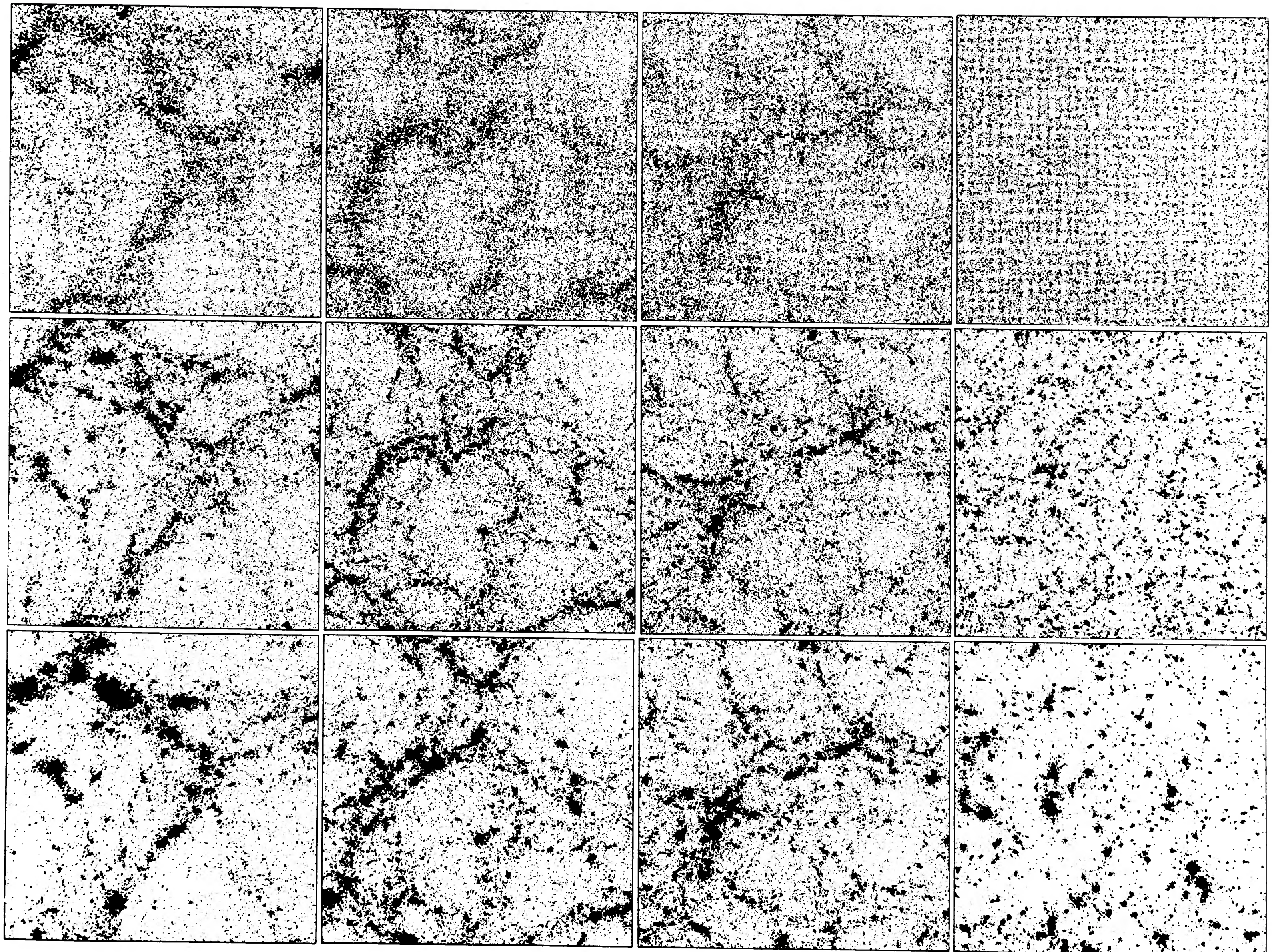

FIG. 1.—Comparison of the four kinds of simulations used in this study. The four columns show CDM models with $L = 2, 10, 32.5h^{-2}$ Mpc, and a white-noise model, respectively. Time advances down the page; top row shows the initial conditions ($a = 1.0$), middle row shows intermediate stages in the calculations ($a = 1.66, 1.68, 1.8$, and 6.07 from left to right), and bottom row shows the stages used in much of our analysis ($a = 2.3, 3.0, 3.0$, and 23.4).

tional field is divided up into long- and short-range components, which are computed by fast Fourier transform and direct summation, respectively. Spatial resolution is limited only by the very short-range force softening introduced to render the equations of motion nonsingular; the two-particle interaction potential $\phi_{\mathrm{P3M}}(r)$ goes exactly as $1/r$ on scales greater than the comoving softening length η and is relatively close to $1/r$ even for separations as small as $\eta/2$ (see Efstathiou *et al.* 1985, Fig. 2). Initial conditions were set up by imposing a chosen spectrum of perturbations on a uniform grid of particles and assigning velocities according to the Zel'dovich (1970) approximation. As Efstathiou *et al.* (1985) show, this procedure yields a good approximation to the desired power spectrum for k between the fundamental wavenumber $k_L \equiv 2\pi/L$ and the Nyquist wavenumber $k_N \equiv N^{1/3}k_L/2$, with perturbations almost entirely in the growing mode.

To explore the dependence of λ on the fluctuation spectrum, we have analyzed 11 models with CDM powerspectra (eq. [3]) and three models with white noise (eq. [1] with $n = 0$). An overview of the simulations is presented in Figure 1: from left to right, we plot three CDM models with computational box lengths $L = 2$, 10, and $32.5h^{-2}$ Mpc, and one white-noise model. The top row shows initial conditions, with time advancing down the page. Parameters for the models analyzed in this study are listed in Table 1; all have $\Omega = 1$, and in each case the softening parameter was $\eta/L = 0.0047$. One CDM model (T0) with a box length $L = 2h^{-2}$ Mpc was run to study tidal torques in a model with a extremely flat fluctuation spectrum; the local spectral index $n(k) \equiv d(\log |\delta_k|^2/d(\log k)$ ranges from $n(k_N) = -2.4$ to $n(k_L) = -2.0$. With so little curvature to the power spectrum, this model is similar to a pure power law with effective spectral index $n_{\mathrm{eff}} = n[(k_N k_L)^{1/2}] \sim -2.2$. As noted by Efstathiou *et al.* (1985), large variations from run to run are expected in models with so much power randomly distributed between the few long-wavelength modes of the computational box. To obtain *statistically* reliable results within a finite computing budget, we chose to concentrate the bulk of our resources on models with somewhat less extreme spectra. We therefore ran an ensemble of five CDM models (S0-4) with $L = 10h^{-2}$ Mpc ($n = -2.2$ to -1.5), providing a large data base for statistical tests. We have also analyzed an ensemble of five CDM models (C0-4) with $L = 32.5h^{-2}$ Mpc ($n = -2.0$ to -0.5), run by DEFW. Comparisons between these two CDM ensembles are of some help in estimating the significance of some of our results. As a foil to the CDM ensembles, we analyzed a pair of white-noise models (W0-1) run by the DEFW group to study self-similar gravitational clustering. In addition, we have reanalyzed the Poisson model (PR1) described by Efstathiou and Barnes (1983).

In our analysis below, we adopt units in which $G = 1$, the mass of each particle $m = 1$, and the comoving computational box length $L = 1$. Comoving and physical lengths will be denoted by x and r, respectively. We use the notation $a(t)$ to denote the cosmological scale factor in our N-body models, normalized to unity at the start of the calculation.

TABLE 1

THE N-BODY SIMULATIONS

Model	N	Spectrum	L	n_{eff}	Amplitude
T0	32768	CDM	2.0	−2.23	1.0
S0–4	32768	CDM	10.0	−1.98	1.0
S0′	8000	CDM	10.0	−1.98	0.822
S0″..........	32768	CDM	10.0	−1.98	0.5
C0–4........	32768	CDM	32.5	−1.59	1.0
W0–1	32768	WN	...	0	1.0
PR1	20000	WN	...	0	1.0

NOTES.—N is the total number of particles. "WN" indicates models with white noise initial conditions, and "CDM" denotes models in which the initial fluctuation spectrum was of the form expected in a cold dark matter universe (eq. [3]). For the CDM models, L denotes the length of the computational box in units of h^{-2} Mpc. Effective spectral index is given by n_{eff} (see § IIIa). Amplitude is that of the initial power spectrum at the Nyquist frequency corresponding to the initial particle grid ($k_N = N^{1/3}\pi/L$) relative to that of a random distribution with the same number of particles.

b) *Group Algorithm*

Locating clusters of particles in the simulations is central to all of the analysis described below. In purely gravitational clustering, there are no well-defined edges or boundaries which delineate the virialized regions from the outer parts of clusters. The outer boundary must therefore be set using an arbitrary crititerion such as mean or local overdensity. Further, we do not want to appeal to special symmetries (e.g., spheres) since clusters have a wide variety of instrinsic shapes. The algorithm that we have adopted was chosen for its computational speed and simplicity. It works by identifying connected regions where the local mass density $\rho(\boldsymbol{x})$ exceeds a fixed threshold without regard to shape. Since the mass distribution in the models is approximated by discrete particles, some local averaging must be used to obtain $\rho(\boldsymbol{x})$. In our procedure, a fixed sphere of radius x_{sph} is placed around each particle, and the particles within that sphere (including the central one) are counted. If there are at least n_{sph} such particles, all particles within the sphere are identified as members of the same cluster. If any of these particles are already members of other clusters, the clusters are merged together. Some details of the algorithm are given in the Appendix. Given values for the parameters x_{sph} and n_{sph}, this procedure maps a distribution of particles into a unique set of disjoint clusters, roughly bounded by surfaces of constant density $\rho_{\mathrm{crit}} = 3n_{\mathrm{sph}}/4\pi x_{\mathrm{sph}}^3$. The algorithm obeys a nesting condition (Efstathiou, Fall, and Hogan 1979) with respect to changes in either x_{sph} or n_{sph}. This property is very useful in assessing the degree of substructure within clusters. If $n_{\mathrm{sph}} = 2$, the algorithm becomes identical to the standard "friends of friends" algorithm (e.g., Davis *et al.* 1985). We have set $n_{\mathrm{sph}} = 4$ and adjusted x_{sph} to give the desired critical density, but our results are not sensitive to this specific choice. Typical large groups identified at a density contrast of $64\bar{\rho}$ are shown in Figure 3 below.

c) *Group Parameters*

For each object identified by the group algorithm we evaluate the following:

1. *Spin parameter* λ, defined by equation (2) in terms of the total angular momentum $\boldsymbol{J}$, energy E, and mass M of a group. Let $\boldsymbol{r}_i$ and $\boldsymbol{v}_i$ be the physical position and velocity of particle i with respect to the group center of mass. All particles have unit mass, so

$$\boldsymbol{J} \equiv \sum_{i=1}^{M} \boldsymbol{r}_i \times \boldsymbol{v}_i \, , \tag{4a}$$

and

$$E \equiv T + U \equiv \frac{1}{2} \sum_{i=1}^{M} |\boldsymbol{v}_i|^2 + \sum_{i=1}^{M} \sum_{j<i} \phi_{\mathrm{P3M}}(|\boldsymbol{r}_i - \boldsymbol{r}_j|) \, . \tag{4b}$$

2. *Principle axes and ellipticities*, computed by diagonalizing the normalized moment of inertia tensor,

$$Q \equiv \frac{1}{M} \sum_{i=1}^{M} r_i \otimes r_i \, . \tag{5}$$

Let $a^2 > b^2 > c^2$ be the principle components of Q, and A the corresponding major-axis vector.

3. *Substructure*, measured by comparing group catalogs defined at different density contrasts. As noted above, the group algorithm obeys a nesting condition, so each group identified at a critical density $\rho_{\rm crit}$ will be resolved into several smaller groups at a higher $\rho'_{\rm crit}$. We parameterize the level of substructure by the quantities f_1 and f_2 which represent the fractional mass in the first and second ranked subgroups, respectively. For example, the group in Figure 3*b* identified at $\rho_{\rm crit} = 64\bar{\rho}$ resolves at $\rho'_{\rm crit} = 512\bar{\rho}$ into two subgoups with fractional masses $f_1 = 0.57$ and $f_2 = 0.11$, with the remaining mass in individual particles and small clumps.

4. *Initial overdensity* $\nu\sigma$, which attempts to quantify the relative amplitude of the linear-regime fluctuation which gave rise to a given object. In our tests of the N-body simulations, we have focused on certain well-defined measures of initial overdensity. The theoretical fluctuation spectra used to generate our initial conditions have no intrinsic short wavelength cutoff, so the small-scale fluctuations are accurately represented apart from particle discreteness. To measure the initial overdensity on the scale of bound clumps, we first smooth the (over)density field $\delta(\boldsymbol{x})$ by convolving with a Gaussian exp $(-x^2/2x_s^2)$; let $\delta(\boldsymbol{x}; x_s)$ be the smoothed overdensity field, with standard deviation $\sigma(x_s)$. We then associate with each particle the value of $\nu = \delta(\boldsymbol{x}; x_s)/\sigma(x_s)$ computed at the particle's initial position $\boldsymbol{x}$. The distribution of ν values within each clump may be used to characterize the initial overdensity, for example, the mean value $\langle \nu \rangle$. These measures depend on the artificial smoothing length, but as we show below, our results for CDM models are largely insensitive to the precise choice. (As $n \to -3.0$, the results are completely independent of x_s).

As an example, the large-scale distribution of high-ν particles in model S0 is shown in Figure 2. We plot particles in groups identified at $a = 3.0$ using $\rho_{\rm crit} = 64\bar{\rho}$ (Fig. 2*a*), particles with $1.0 \leq \nu \leq 2.0$ defined for a smoothing length $x_s = 1/64$ (Fig. 2*b*), and particles with $\nu \geq 2.0$ at $a = 3.0$ (Fig. 2*c*), and in the initial conditions (Fig. 2*d*). These plots may be compared to the corresponding frames in Figure 1 (col. [2]). The enhanced

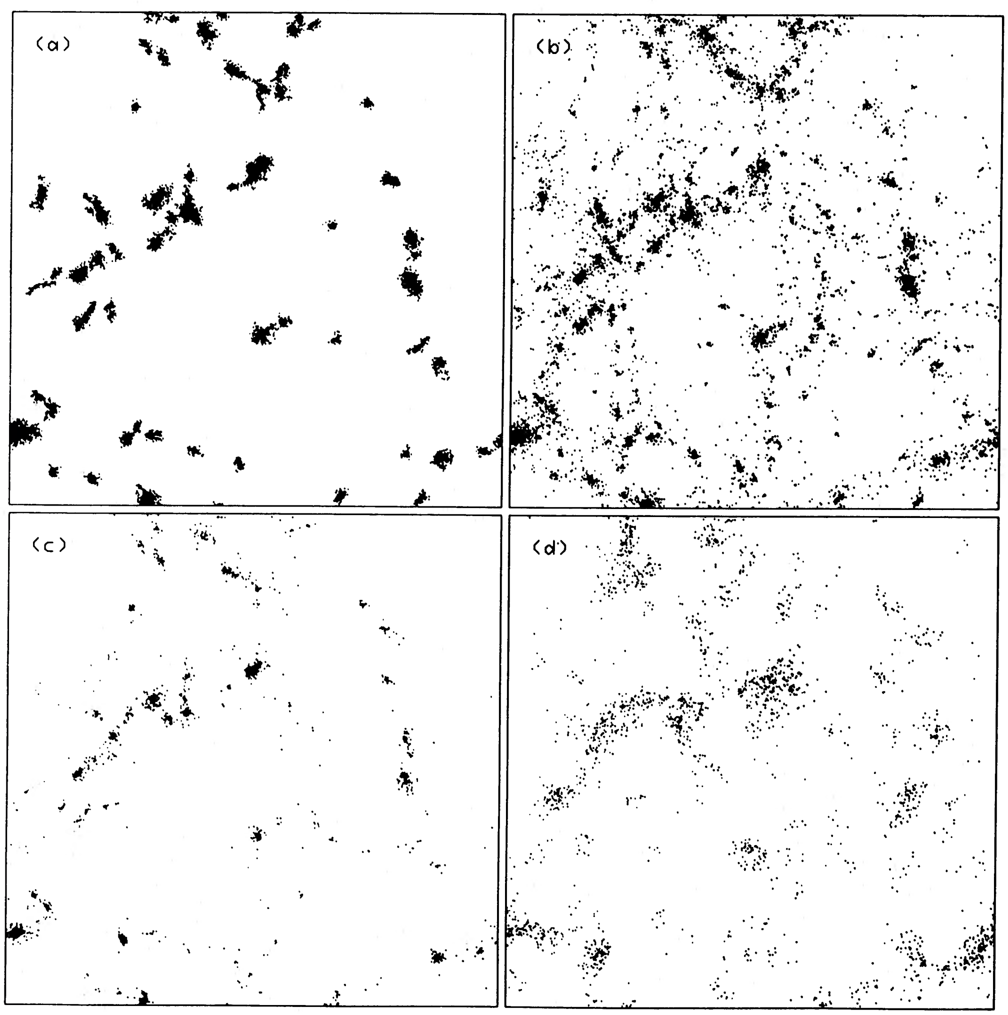

FIG. 2.—Large-scale distribution of particles in groups and above various thresholds in model S0. (*a*) Particles assigned to groups above $64\bar{\rho}$. (*b*) Particles with $1.0 < \nu < 2.0$. (*c*) Particles with $\nu > 2.0$ at $a = 3.0$. (*d*) Initial positions of these particles.

clustering of particles with high ν predicted by Kaiser (1984) is clearly seen. The figure also shows the close correspondence between high-ν particles and the prominent groups.

III. INDIVIDUAL OBJECTS

In this section we describe the properties of a few objects in some detail to provide physical insight into the tidal torque mechanism. We focus our discussion on the five most massive groups identified at a density contrast of $\rho_{\rm crit} = 64\bar{\rho}$ in simulations T0 (at $a = 2.34$), S0 ($a = 3.0$) and in W0 ($a = 23.4$). These particular simulations were chosen to test whether our results are sensitive to initial conditions; as is evident from Figure 1, the initial fluctuation spectra in these three models differ substantially. We have restricted the analysis to massive groups because they have the best resolved internal structure. This introduces a distinct selection bias of which the reader should be aware. It is not really possible to assess in detail how certain group properties, e.g., the variation of specific angular momentum with radius, depend on mass. Less massive objects simply do not contain enough particles to allow a detailed analysis of their internal structure. The analysis of this section will be complemented by a statistical study in § IV of the *global* properties of groups spanning a wide range of masses. In § III*a* we describe the density structure of these groups, and in § III*b* we discuss the spatial distribution and evolution of angular momentum. In § III*c* we investigate the range of the local tidal field for the various initial density fields in our simulations.

a) Structure of Massive Groups

On the left-hand panels in Figure 3, we show particle positions for groups T0(4), S0(5), and W0(2) respectively. [The notation T0(4), for example, denotes the fourth most massive group in simulation T0]. Points belonging to the first- and second-ranked subgroups identified at $\rho_{\rm crit} = 512\bar{\rho}$ are plotted as circles and crosses, respectively; the remaining points are plotted as dots. The diagrams in the right-hand panels show "smoothed" representations of these groups: the ellipsoids shown in these figures were constructed with the same orientations and axial ratios, computed from eq. (5). Some key parameters for these groups are listed in Table 2.

These groups are quite typical of the large groups in our simulations. Some are centrally concentrated, with one prominent subcluster [e.g., W0(2)], while others [e.g., S0(5)] contain several distinct subclumps. On the right-hand panels of Figure 3 we have indicated the directions of the angular momentum vectors for the larger subclusters and for the groups as a whole. The spins are fairly well aligned in group W0(2), while in contrast the angular momentum of the two large subgroups in S0(5) point in roughly opposite directions. These spin alignments will be discussed further in § III*b*.

In Figure 4 we show "circular" velocity profiles $v_c(x) = [GM(x)/x]^{1/2}$ for our 15 selected groups. Here $M(x)$ is the total mass of all particles within a sphere of radius x centered on the group, including those which were explicitly assigned to the group. The precise definition of the group "center" has an important bearing on the results. We do not use the center of mass of the whole group, since this is offset from any center of mass concentration if significant substructure is present. The resulting "circular" velocity profiles would then appear to have spuriously large cores. Instead, we have computed the potential energy of each particle in the first ranked subgroup identified at $\rho_{\rm crit} = 512\bar{\rho}$ and identified the center of the group as the location of the most tightly bound particle. The reality of

TABLE 2

PROPERTIES OF MASSIVE GROUPS

Group	M	f_1	f_2	λ	$T/\lvert W\rvert$	θ_{1R}	θ_{2R}
			$a = 2.34$				
T0(1)	2598	0.197	0.099	0.097	0.48	121.9	40.1
T0(2)	749	0.267	0.069	0.091	0.54	45.8	6.6
T0(3)	608	0.538	0.041	0.074	0.59	14.0	50.2
T0(4)	570	0.465	0.079	0.054	0.61	110.2	77.8
T0(5)	565	0.543	0.021	0.033	0.58	68.2	48.7
			$a = 3.0$				
S0(1)	870	0.522	0.018	0.035	0.58	79.8	35.1
S0(2)	676	0.450	0.053	0.034	0.62	11.6	101.7
S0(3)	546	0.589	0.048	0.046	0.59	61.2	12.3
S0(4)	476	0.431	0.052	0.027	0.54	105.2	135.8
S0(5)	425	0.574	0.111	0.031	0.65	88.5	108.7
			$a = 23.4$				
W0(1)	1209	0.508	0.070	0.049	0.52	75.8	21.1
W0(2)	986	0.720	0.052	0.035	0.60	19.7	66.9
W0(3)	975	0.567	0.048	0.035	0.52	41.7	109.3
W0(4)	639	0.622	0.094	0.089	0.57	17.1	133.6
W0(5)	576	0.712	0.021	0.035	0.56	77.3	93.1

NOTES.—M denotes the total number of particles per group at $\rho_{\rm crit} = 64\bar{\rho}$; f_1 and f_2 give the fraction of the total group mass in the first- and second-ranked subgroups, respectively, where the subgroups were identified with $\rho_{\rm crit} = 512\bar{\rho}$; λ is the spin parameter λ, $T/|W|$ is the ratio of the kinetic to potential energy; θ_{1R} and θ_{2R} give the directions between the angular momenta of the first- and second-ranked subgroups, respectively, related to the angular momentum of the rest of the particles in the group.

the resulting cores shown in Figure 4 is compromised primarily by the effective softening ($\sim\eta/2$) in the P3M potential, which is indicated by the arrows in the figure.

These results show that $v_c(x)$ for clumps in the CDM–like models is very nearly flat, while $v_c(x)$ in the white noise model falls slowly with x (approximately as $x^{-0.25}$). The outermost point of each curve corresponds to the radius at which the average density exceeds that of the mean background by a factor $\Delta = 100$. The large cores in models T0 and S0 are probably significant, while those for some of the groups in model W0 are of the same size as the effective potential softening. The density profiles of the large groups in models T0 and S0 are similar to those inferred for the dark halos around spiral galaxies (e.g., Rubin *et al.* 1985, and references therein), while those in model W0 fall somewhat too steeply. Similar results have been obtained by Frenk *et al.* (1985) for CDM models and by Quinn, Salmon, and Zurek (1986) for a set of scale-free models. It is beyond the scope of this paper to make a more detailed comparison between the density profiles of dark halos and those of the N-body groups. Briefly, the main problem with such a comparison lies in scaling the models to physical units. This can be done is several ways. For example, one can match the amplitude of the observed two-point galaxy correlation function $\xi(r)$ or its second moment $J_3(r)$ (Peebles 1974, 1981) with corresponding results from the simulations. However, this has the disadvantage that an extrapolation to small scales ($< 20h^{-1}$ kpc) is required to compare with the properties of dark halos. A more direct approach is to match the inferred density contrast for halos on length scales similar to those over which spiral rotation curves are measured. For a flat rotation curve, the overdensity interior to radius r relative to an $\Omega = 1$ background is $\Delta = 2v_c^2/(H_0 r)^2$. For a typical large spiral ($L \approx 5 \times 10^{10}\ L_\odot$), $\Delta \approx 1 \times 10^4$ within a Holmberg

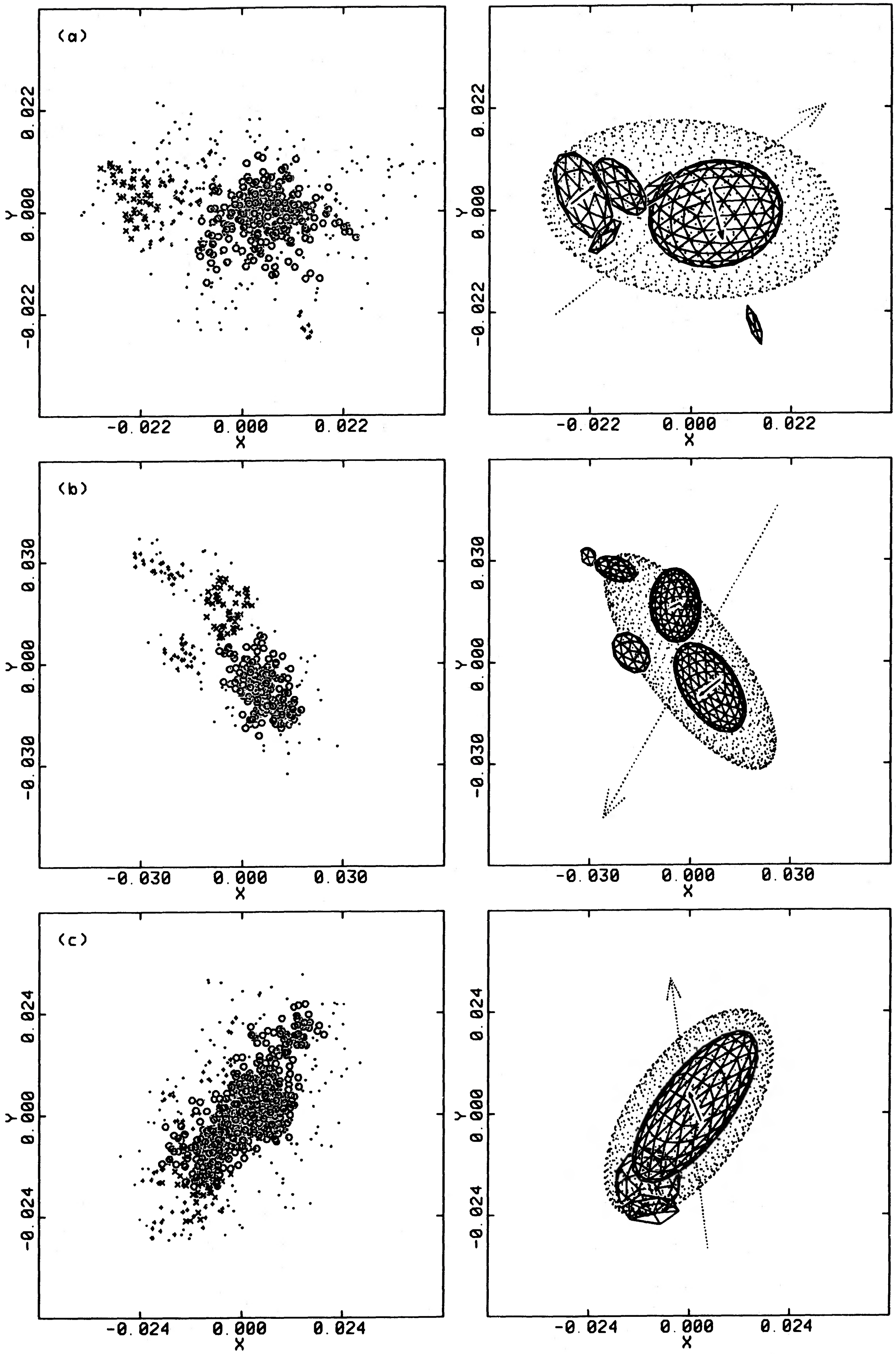

FIG. 3.—Internal structure of several massive groups identified in models T0, S0, and W0. In the notation defined in § IIIa, (a) shows group T0(4), (b) shows S0(5), and (c) shows W0(2). In the left-hand panels the positions of particles belonging to the first-ranked subgroup ($\rho_{crit} = 512\bar{\rho}$) are shown as open circles, those belonging to the second-ranked subgroups as crosses, and the remaining particles as dots. The right-hand panels show smoothed representations of the groups in which groups and subgroups are represented by ellipsoids. In each case, we have indicated the orientation of the angular momentum of the group and those of the two largest subclumps.

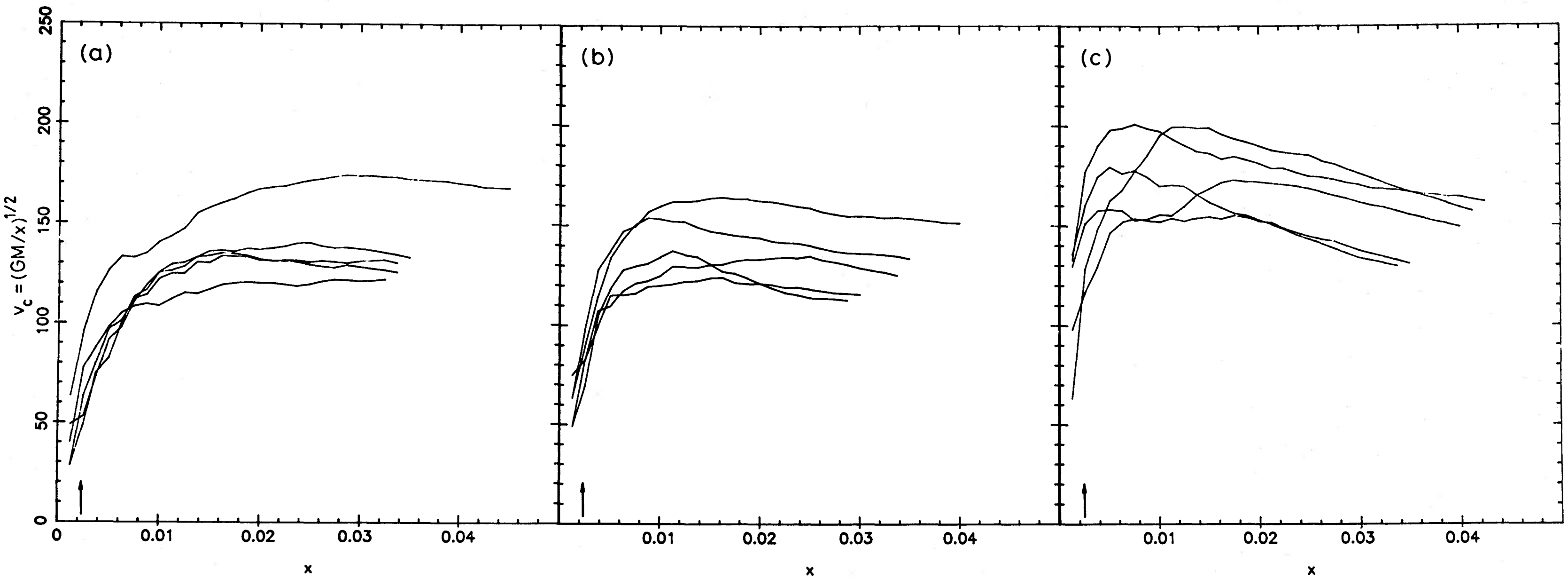

FIG. 4.—Plots of the "circular" velocity $v_c = [GM(x)/x]^{1/2}$ as a function of comoving distance x from the center of each of the five most massive groups in models (*a*) T0, (*b*) S0, and (*c*) W0. Arrows show the effective softening length of the P3M force law ($\eta/2$; see § II*a*).

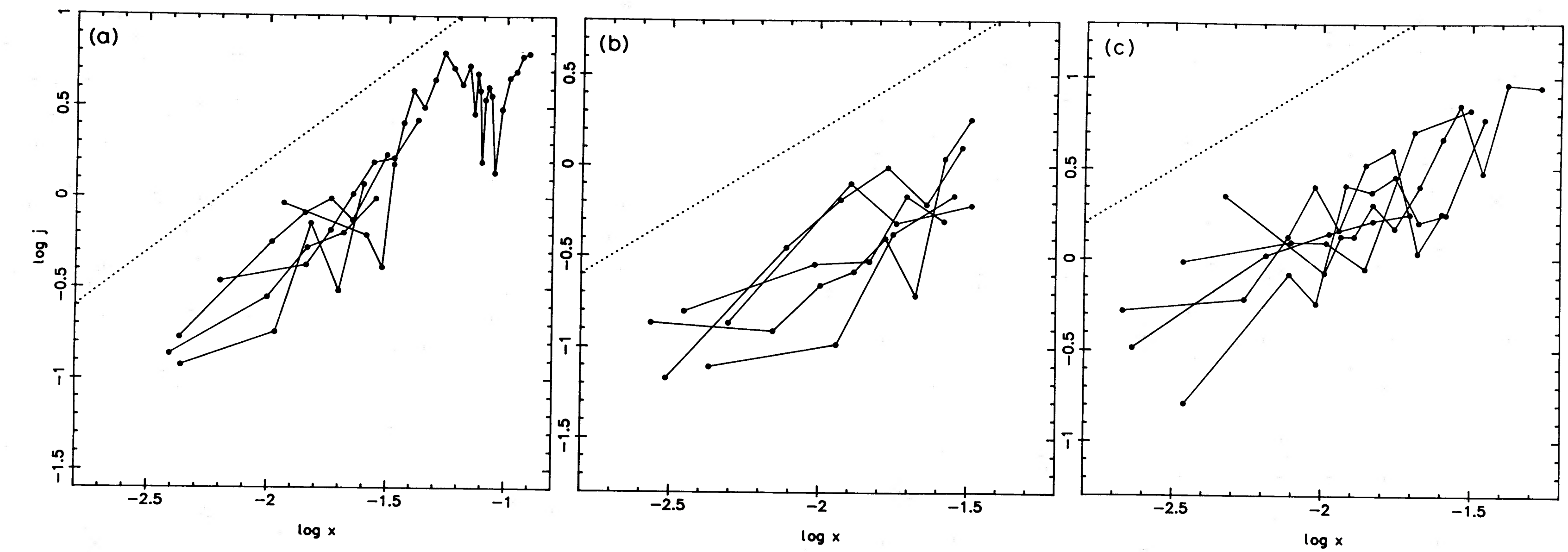

FIG. 5.—Plots of the variation of specific angular momentum with distance from the center of mass for the massive groups in models (*a*) T0, (*b*) S0, and (*c*) W0. Dashed lines show the relation $j(x) \propto x$.

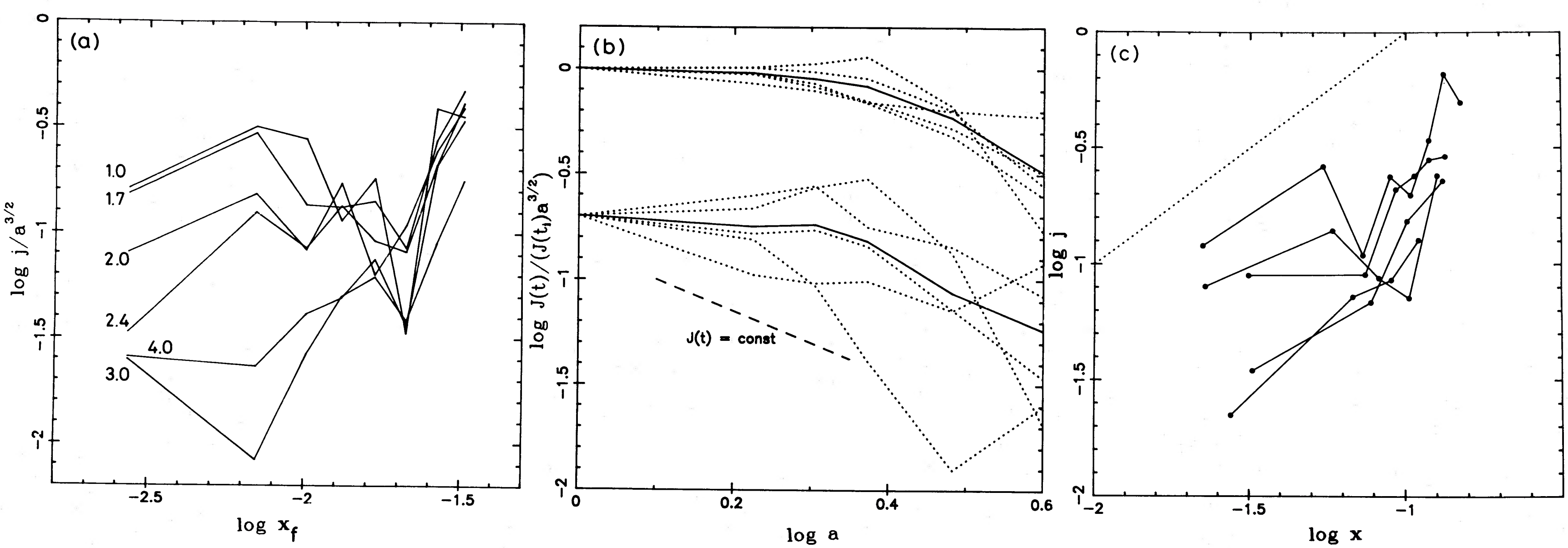

FIG. 6.—Evolution of angular momentum for groups in model S0. (*a*) Evolution of the specific angular momentum in group S0(1) for particles in Lagrangian shells with "final" ($a = 3.0$) radius x_f. (*b*) Time evolution of the angular momentum for the five most massive groups in model S0. Upper dotted curves show $J(t)/[J(t_i)a^{3/2}]$ for particles belonging to groups identified at $a = 3.0$ with $\rho_{\rm crit} = 64\bar{\rho}$; lower curve shows $J(t)/[J(t_i)a^{3/2}]$ (divided by a factor of 5 to preserve clarity in the figure) for the largest subgroup identified at $a = 3.0$ with $\rho_{\rm crit} = 512\bar{\rho}$. In each case the heavy line shows the mean of the dotted curves. (*c*) Initial spatial distribution of angular momentum in the massive groups. Dashed lines show the relation $j(x) \propto x$.

radius ($r_H \approx 30h^{-1}$ kpc), while for a small spiral ($L \approx 3 \times 10^9$ $L_\odot$), $\Delta \approx 1 \times 10^5$ within $r_H \approx 6h^{-1}$ kps (see Fall and Efstathiou 1980, Table 1). At the radius defined by the effective softening ($\eta/2$) in Figure 4 the most massive clumps in model W0 have $\Delta \approx 4 \times 10^4$, while those in models S0 and T0 have $\Delta \approx 1 \times 10^4$. Thus, there is marginal overlap between observations of the largest spirals and the N-body results presented here. This agrees with Figure 2 of Frenk *et al.* (1985), who used a self-consistent scaling adopted from their earlier work on large-scale structure in CDM models (DEFW), and with the results of Quinn *et al.*, who adopted a scaling for which their N-body integrations have a resolution of $\sim 10h^{-1}$ kpc. Additional ambiguities in comparing N-body results with observed rotation curves arise from the possibility that the collapse of a luminous component might alter the distribution of dark matter in the central regions of a halo.

b) *Internal Distribution and Evolution of Angular Momentum*

In Figure 5 we show the specific angular momentum $j(x)$ for our selected groups computed in shells as a function of radius from the center of mass. The bins were chosen so that they each contain 100 particles. For each set of initial conditions the specific angular momentum of material in the inner regions of the groups is substantially lower than in the outer parts. The dotted lines in each panel show the relation $j(x) \propto x$, which provides a reasonable approximation to the results. It is instructive to examine how this distribution of angular momentum arises. We have therefore calculated the evolution of the specific angular momentum for the particles belonging to each of the radial bins used in Figure 5. A typical example of this evolution is shown in Figure 6*a*, where we plot results for the group S0(1). At the time the simulation begins, the distribution of j is nearly constant, and the material which is destined to clump toward the center of a group has almost the same specific angular momentum as that which ends up in the halo. As the evolution proceeds, $j(x)$ of the inner material begins to grow at a slower rate than that for the halo material, and at $a > 2$ angular momentum is lost from the central regions. The growth rate of the angular momentum in linear perturbation theory can easily be derived using the Zel'dovich (1970) approximation for particle trajectories. This states that

$$r = a(t)x = a(t)[q + b(t)p(q)] \ , \quad p(q) = -\nabla\psi \ , \qquad (6)$$

where q is the initial unperturbed particle coordinate and $b(t) \propto a(t) \propto t^{2/3}$ if $\Omega = 1$. As shown by Doroshkevich (1970) and White (1984), the angular momentum of the material in a Lagrangian volume,

$$J(t) = \int \bar{\rho} a^5 (x - \bar{x}) \times \dot{x} d^3 q$$

(where $\bar{x}$ denotes the center of mass and dots denote derivatives with respect to t) may be approximated to first order using equation (6) as

$$J(t) \approx \bar{\rho} a^5 \int (q - \bar{q}) \times p(q) d^3 q \ . \qquad (7)$$

Thus according to linear perturbation theory we expect

$$J(t) \propto a^{3/2} \propto t \qquad (8)$$

in an $\Omega = 1$ universe. This derivation is rigorous only if the mass distribution is linear on all scales. If the distribution is nonlinear, it is possible that small-scale motions could alter the growth rate of J even if the integral in equation (7) extends over a volume which encloses a small net density perturbation. A description of this type of mode coupling effect is beyond these scope of linear perturbation theory and at present can be investigated only by N-body simulations. White (1984) showed that such effects are unimportant in simulations with white noise or "massive neutrino" initial conditions. A similar comparison is shown in Figure 6*b* for the five largest groups in model S0. The top set of dashed curves shows the evolution of $J(t)$ for each group identified at the standard density contrast $\rho_{\rm crit} = 64\bar{\rho}$ at $a = 3.0$. The lower set of dashed curves show $J(t)$ for the largest subgroup ($\rho_{\rm crit} = 512\bar{\rho}$) in each group. The early evolution is in excellent agreement with the linear theory prediction. As the clumps become nonlinear, the growth rate of $J(t)$ decreases on average. It is easy to see why this occurs. The torque on a set of particles G is

$$\Gamma = \frac{1}{a} \sum_{i \in G} \sum_{j \notin G} \frac{x_i \times x_j}{|x_i - x_j|^3} \ , \qquad (9)$$

where the origin of the coordinates in equation (9) is chosen to be the center of mass of G. Now according to the Zel'dovich approximation, the force on a particle is $F_i = a(a^2\dot{b})^{\cdot} p(q_i)$. Thus in linear theory equation (9) gives $\Gamma = (a^2\dot{b})^{\cdot} \Sigma(q_i - \bar{q}) \times p(q_i)$ = constant in agreement with equation (7). As an idealized model of nonlinear evolution, consider the case when the mass distribution within the clump G ceases to evolve in proper coordinates while the forces from external sources continue to grow at the linear rate. The torque will then decrease as $\Gamma \propto t^{-2/3}$. This model is intended to describe the way in which a nonlinear clump might decouple from the tidal field. In fact, the real behavior is considerably more complex. The curves in Figure 6*b* show that the evolution of $J(t)$ becomes extremely erratic when clumps become highly nonlinear. Some clumps loose a large fraction of their angular momentum within a short time interval, while $J(t)$ for other clumps continues to grow relatively smoothly, although at a slower rate then predicted by linear theory. In particular, notice that for two high-density subgroups $J(t)$ falls substantially between $a = 2.0$ and $a = 3.0$, but their angular momentum increases sharply between $a = 3.0$ and $a = 4.0$. The explanation for this behavior is apparent from Figure 7 which shows the time evolution of all the particles belonging to group S0(5) together with those of the two largest subgroups. Table 3 lists the time evolution of the angular momentum of the whole group (J_T), those of the first- and second-ranked subgroups (J_1 and J_2, respectively, defined relative to their center of masses) and the orbital

TABLE 3

EVOLUTION OF J FOR GROUP S0(5) AND TWO LARGEST SUBGROUPS

a	J_T	J_1	J_2	J_{01}	J_{02}	$\Delta\theta_T$	$\Delta\theta_1$	$\Delta\theta_2$
1.00	37.8	15.9	1.2	7.0	8.8	0.0	0.0	0.0
1.68	83.8	37.7	3.5	11.7	19.8	9.2	14.6	34.5
2.02	115.0	62.5	7.8	6.1	35.9	12.2	23.0	55.4
2.36	156.7	87.0	7.9	9.2	42.5	21.7	23.0	57.5
3.04	133.4	56.5	7.5	39.4	42.3	20.4	28.2	64.2
4.04	47.9	12.0	43.1	22.4	37.9	32.0	58.7	77.9

NOTES.—Cosmological scale factor is denoted by a; J_T is the total angular momentum of group S0(5), J_1 and J_2 list the internal angular momenta of the two largest subgroups (see § III*b* for details). The orbital components of the subgroups relative to the center of mass of the whole group are given by J_{01} and J_{02}; $\Delta\theta_T$, $\Delta\theta_1$, and $\Delta\theta_2$ denote the change in direction of the angular momenta J_T, J_1^2, and J_2 respectively, relative to their initial directions at $a = 1$.

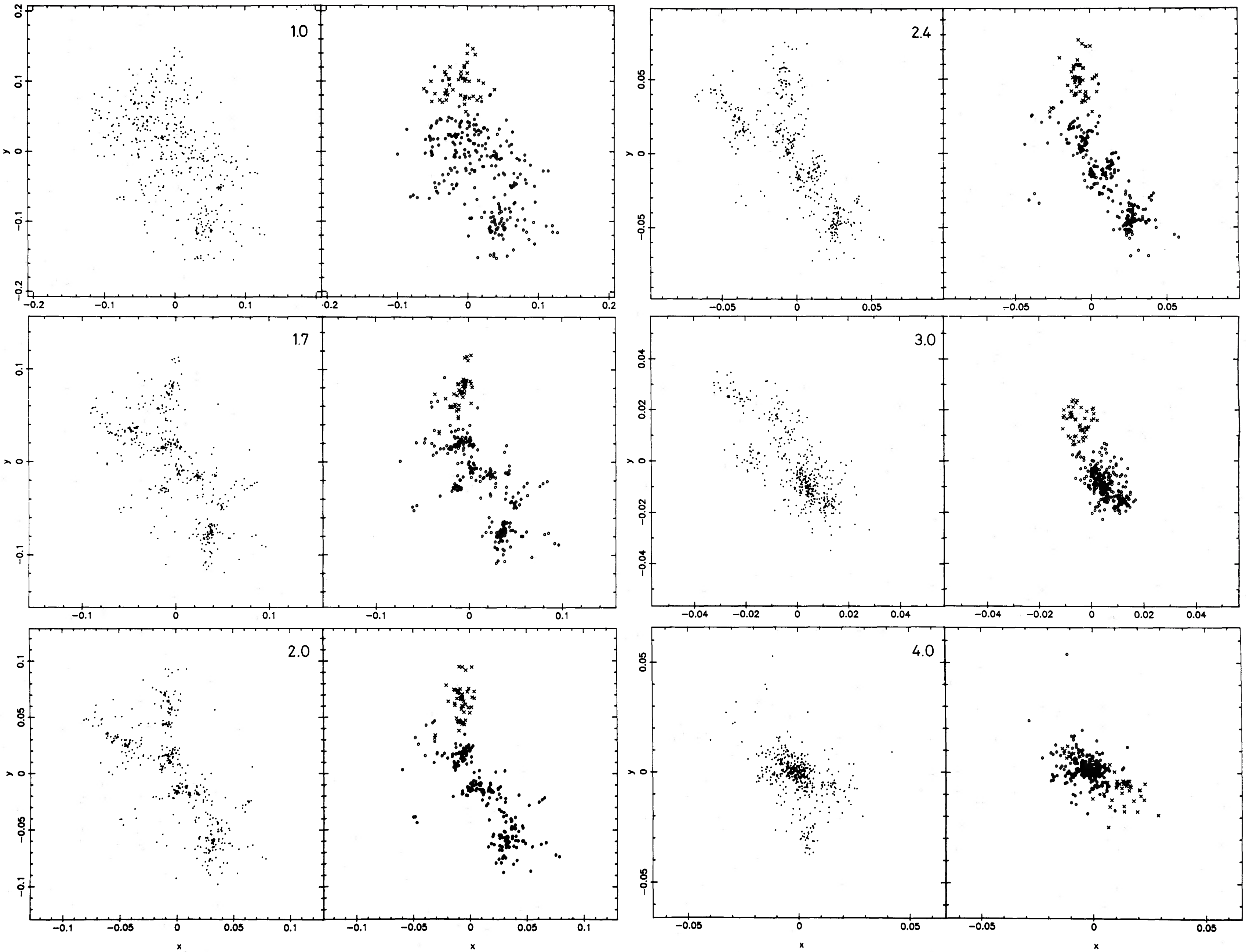

FIG. 7.—Evolution of group S0(5). The cosmological scale factor a is indicated for each pair of diagrams. Left-hand member of each pair shows the position of each particle belonging to group S0(5), and right-hand member shows only particles belonging to the first- and second-ranked subgroups. As in Fig. 3, open circles show particles belonging to the first-ranked subgroup, and crosses show particles belonging to the second-ranked subgroup.

angular momenta of each subgroup relative to the center of mass of the whole group (J_{01} and J_{02}, respectively). In addition, we list three angles which indicate how the spin directions change with time: $\Delta\theta_T = \cos^{-1}[\hat{\boldsymbol{J}}_T(t) \cdot \hat{\boldsymbol{J}}_T(t_i)]$, $\Delta\theta_1 = \cos^{-1}[\hat{\boldsymbol{J}}_1(t) \cdot \hat{\boldsymbol{J}}_1(t_i)]$, and $\Delta\theta_2 = \cos^{-1}[\hat{\boldsymbol{J}}_2(t) \cdot \hat{\boldsymbol{J}}_2(t_i)]$. The plot of the particle positions in Figure 7 shows that the group first breaks up into a number of small clumps which subsequently merge to form a nearly featureless structure by $a = 4$ (see Frenk *et al.* 1985; White 1976). These subclumps loose orbital angular momentum to surrounding material as they merge, and it is this process that accounts for the general tendency for angular momentum to fall when groups become highly nonlinear. For group S0(5) shown in Figure 7, the internal angular momentum vector $\boldsymbol{J}_1$ of the dominant subgroup at $a = 3$ is of similar magnitude to that of its orbital angular momentum $\boldsymbol{J}_{01}$ (Table 3), and the two vectors are aligned to within 19°. By $a = 4$, $\boldsymbol{J}_{01}$ has nearly reversed direction ($\Delta\theta = 170°$), and its magnitude has fallen by nearly a factor of 2. In this time interval, the magnitude of $\boldsymbol{J}_1$ fell by a factor of 4, and its direction changed by 60°, while the internal angular momentum of the second-ranked subgroup $\boldsymbol{J}_2$ increased by a factor of nearly 5, and its direction changed by 56°. However, the large decrease in the total angular momentum of the group is dominated by the combined change in the orbital angular momenta $\boldsymbol{J}_{01}$ and $\boldsymbol{J}_{02}$. The angular momentum of particles that are not members of the two largest subclumps suffers a relatively small change between $a = 3$ and $a = 4$, with the magnitude increasing from 92.9 to 93.5 and the direction changing by only 23°.5. Most of this change is due to transfer of the x components of the orbital angular momenta of subclumps 1 and 2 to this material. The rest of the change in the orbital angular momenta is absorbed by material external to the group.

The decay of orbital angular momentum is a general feature of the evolution of groups in our numerical simulations. The erratic nonlinear evolution of the internal angular momenta of subclumps illustrated in Figure 6*b* is of less general interest. This is because the subgroups are identified as distinct objects at a specific epoch, and they may not retain their identity at later times. As may be seen in Figure 7, at $a = 4$ the second-ranked subgroup no longer corresponds to a single well-defined density concentration but has been sheared out into a long structure and in the process has gained a large amount of internal angular momentum. When the evolution of a group becomes highly nonlinear, the internal angular momenta of subclumps can suffer large changes of either sign since the torque is dominated by the presence of nearby nonlinear lumps (see § III*c*).

As indicated by the preceding discussion, the direction of the angular momentum vector of material near the center of a group may be poorly correlated with that of material in the outer parts. In Table 2, we list the direction between the angular momenta of the first- and second-ranked subgroups with respect to the angular momentum of the rest of the particles in the group. This shows that large misalignments are relatively common. We have also investigated the variation of the orientation of the angular momentum measured in spherical shells relative to the group center of mass. In general, we find that the spin direction of material with density contrast $\Delta \gtrsim 500$ is poorly aligned with that of the halo material. The spin directions of shells of material with lower density contrasts are often well aligned (to within 30°), but large deviations, which are usually associated with substructure, may occur. (Note that these results are insensitive to the exact choice of the group center.) In the tidal-torque picture one must therefore expect that the direction of the angular momentum vector of infalling material will vary in a complex way with distance from the center of a protogalaxy. These variations will depend in detail on the internal structure of the protocloud. Binney and May (1986) have recently discussed some of the consequences of such misalignments for the evolution of galactic spheroids.

We have checked carefully that the results given above are not sensitive to particle discreteness. As a quantitative example, consider the internal distribution of angular momentum at $a = 3.0$ illustrated in Figure 6*a* for the group S0(1). From each radial bin we have removed the 10 particles with the largest angular momenta (i.e., 10% of the total number of particles per bin). In the innermost bin, the total angular momentum decreases by 24%, and the spin direction changes by 22°. In the outermost bin, the magnitude of $\boldsymbol{J}$ decreases by 19%, and the orientation changes by 21°. These results are quite typical of those for the massive groups described in this section and illustrate that the angular momenta are not unduly sensitive to the inclusion or exclusion of a few particles.

It has sometimes been stated that the tidal torque process ought to yield protoclouds in approximately "solid-body" rotation, $j(x) \propto x^2$ (Gott 1975; Gott and Thuan 1976; Thuan and Gott 1977). Since this differs from the behavior $j(x) \propto x$ shown in Figure 5, it is worth reviewing the cause of the discrepancy.

Gott's (1975) argument can be rephrased as follows. The angular momentum of a particle may be written to first order in linear perturbation theory as

$$\boldsymbol{j} = a^2\dot{b}(\boldsymbol{q} - \bar{\boldsymbol{q}}) \times [\boldsymbol{p}(\boldsymbol{q}) - \boldsymbol{p}(\bar{\boldsymbol{q}})] .$$

Expanding $\boldsymbol{p}(\boldsymbol{q})$ as a Taylor series about $\boldsymbol{q}$ gives

$$j_\alpha(\delta\boldsymbol{q}) \approx -(a^2\dot{b})\epsilon_{\alpha\beta\gamma}\,\delta q^\beta \delta q^\kappa \psi_{,\kappa,\gamma} , \tag{10}$$

where $\delta q^\alpha = q^\alpha - \bar{q}^\alpha$ and the second derivative of ψ is evaluated at $\bar{\boldsymbol{q}}$. The angular momentum of a particle thus varies as the second power of the initial displacement $\delta\boldsymbol{q}$. However, if we integrate equation (10) over a spherical Lagrangian volume, the total angular momentum vanishes identically. If we perform a similar analysis for the angular momentum in a spherical Eulerian volume, we find to lowest order

$$\begin{aligned} J_\alpha &= a^5\epsilon_{\alpha\beta\gamma}\int [\rho(u^\gamma - \bar{u}^\gamma)]_{,\kappa}\,\delta x^\kappa \delta x^\beta d^3\boldsymbol{x} \\ &= -a^5\,\frac{4\pi}{15}\,x^5[\boldsymbol{u}(\bar{x}) - \bar{\boldsymbol{u}}] \times \nabla_x \rho|_{\boldsymbol{x}=\bar{\boldsymbol{x}}} , \end{aligned} \tag{11}$$

where $\boldsymbol{u} = \dot{\boldsymbol{x}}$ (see also Peebles 1980, § 23). The total angular momentum in the Eulerian sphere therefore depends critically on the level of inhomogeneity of the protocloud (see Binney 1974). These arguments show that the angular momentum distribution of a cluster in linear perturbation theory is determined by the precise initial spatial distribution of the particles of which it is comprised. Thus, although the argument presented by Gott (1975) that the angular momentum of a particle should scale approximately as δq^2 is qualitatively correct, its subsequent interpretation (Gott and Thuan 1976; Thuan and Gott 1977) that it implies uniformly rotating ($\boldsymbol{v} = \boldsymbol{r} \times \boldsymbol{\omega}$, ω = constant) protoclouds is erroneous. In Figure 6*c*, we show the initial specific angular momentum $j(x)$ computed in shells as a function of the initial radial distance from the center of mass for the five massive groups from model S0. The dotted line shows the relation $j(x) \propto x$. The results for groups in simulations T0 and W0 are similar. Thus, the initial distribution of angular momentum scales with separation in a similar fashion to that found above for well-developed groups (Fig. 5). It is important to link this result with our discussion of Figure 6*a*, which shows how the angular momentum distribution in a typical clump evolves. We remarked above that there is no strong correlation between the initial specific angular momentum and the final location of a particle within a clump. However, Figure 6*c* clearly shows that material which lies initially close to the center of the clump has lower specific angular momentum than that in the outer parts. These results are not incompatible since the particles which eventually reach the core of a clump are only marginally more centrally concentrated at the initial time than those which end up in the halo. Substantial radial mixing occurs as a clump evolves.

Crampin and Hoyle (1964) made the interesting observation that the distribution of angular momentum in disk galaxies is similar to that of a uniform sphere in uniform solid body rotation. An extension of this argument has been presented by Fall and Efstathiou (1980), who investigated the formation of disk galaxies in a two-component model containing gas and nondissipative dark matter (see White and Rees 1978). They assumed that in the early stages of protogalactic evolution the gas and the dark material would behave as one single component, with similar radial density profiles and distributions of specific angular momentum. In their model, the two components would "separate" as the system becomes nonlinear, with the dark material settling down to a roughly isothermal form while the gas dissipates and collapses to a disk. Using modern photometric and kinematic data for disk galaxies, they showed that the angular momentum distribution within spiral disks is similar to that of an "isothermal" ($\rho \propto 1/r^2$) sphere in which the specific angular momentum varies approximately as $j(r) \propto r$. (Note that their assumption of cylindrical rotation rather than spheroidal rotation does not significantly alter this conclusion.) These properties are similar to those described above for evolved groups in our simulations (i.e., groups identified at $\rho_{\rm crit} = 64\bar{\rho}$). This similarity could be used as support for the basic theory if each element of material in a protocloud conserved its angular momentum during and after collapse. However, as we have shown above, nonlinear torques play an important role in determining the angular momentum distribution within a group. It is therefore difficult to assess exactly how these effects would modify the angular momentum distribution of the gaseous component since they depend critically on the spatial distribution of the gas and thus on the rate at which dissipation occurs. Some aspects of this problem will be discussed in § V.

c) The Tidal Field

In this section we investigate whether our simulations have sufficient dynamic range to model the tidal field correctly. Our models clearly do not include perturbations with wavelengths larger than the computational box. It is therefore important to check whether the absence of long-wavelength perturbations significantly affects the total torque acting on the groups. The following argument suggests that this is unlikely to be a significant problem. The tidal field is given by $T_{ij} = \phi_{,i,j} \propto \Sigma \delta_k (k_i k_j / |k|^2) e^{i\mathbf{k} \cdot \mathbf{x}}$. The expectation value $\langle T_{ij} T_{ij} \rangle$ at any point is thus proportional to $\int |\delta_k|^2 k^2 dk$, which is dominated by short-wavelength perturbations unless $n \leq -3$. Figure 8 shows how the initial torque (at $a = 1$) on the massive groups in our models converge with increasing scale. The quantity $\Gamma(x)$ represents the torque from all material within a radius x from the center-of-mass of the group and has been computed using equation (9). Since linear theory predicts Γ = constant (eq. [8]), we expect the total torque to be related to the initial angular momentum of our groups according to $J(t_i) = \Gamma t_i$. The typical initial radii of the groups lie in the range $0.1 < x < 0.2$ (see Fig. 7); thus, there is little contribution to the torque on these scales from other particles. For the white-noise model (W0, Fig. 8*c*), and the $L = 10h^{-2}$ Mpc CDM model (S0, Fig. 8*b*), the torque converges rapidly with increasing scale. On average, there is little torque from material at $x > 0.3$. The quantity $\Gamma(x)$ is nearly flat from $x \approx 0.3$ to the boundary of the calculation at $x = 0.5$, and the ratio $\Gamma(x)t_i/J(t_i)$ tends to unity as expected from linear theory. We therefore conclude that for typical groups in models W0 and S0 the dominant contribution to the torque arises from material close to the group. The neglect of longer wavelength perturbations should not significantly bias our results on angular momentum from these simulations.

Figure 8*a* shows results from model T0 which was set up to model a CDM spectrum with a computational box length of $L = 2h^{-2}$ Mpc. The spectrum has substantial power at large scales, and we might anticipate that the long-wavelength contribution to the torques might not be modeled correctly. Indeed, we see that $\Gamma(x)$ in this case does not converge as rapidly as in models S0 and W0. The rms torque for these groups increases steadily until $x = 0.4$. However, between $x = 0.4$ and $x = 0.5$ the rms torque increases by only 12%. At $x = 0.5$, the mean value of $\Gamma t_i/J(t_i)$ is slightly smaller than unity, showing that the simulation boundaries are noticeably affecting the results. Recall that our numerical procedure for solving for the potential employs triply periodic boundary conditions. The total torque on a group thus includes the contribution from an infinity of images. From Figures 8*b* and 8*c* we see that the presence of images does not significantly affect the angular momentum acquired by groups in models S0 and W0.

The spectrum adopted in model T0 is probably close to the limit at which reliable results for group angular momentum can be derived using our numerical techniques. It is difficult to make an accurate assessment of the error introduced from the missing long wavelengths, but Figure 8*a* suggests that it is probably small, the torques have already converged to within 20% by $x = 0.4$, and the contribution from more distant material and images are smaller than 10%, on average. Thus we suspect that the λ parameters for groups in model T0 are probably accurate to $\sim 20\%$. The median value of λ for groups in this model is $\lambda_{\rm me} = 0.047$, which is not unusually low in comparison with the results from, say, models S0–4 (see § IV*a*).

One way of including long-wavelength perturbations, without an enormous increase in computational expense, might be to split the interparticle force into two components: a short-range component computed using standard *N*-body techniques, and a long-range component generated directly from the desired power spectrum which is assumed to grow according to linear perturbation theory. Such a hybrid scheme may be worth investigating as a way of extending the results presented in this paper.

In § III*b* we mentioned that when groups become highly nonlinear, the main contribution to the external torque comes from nearby nonlinear clumps. In other words, the contribution from long-wavelength perturbations becomes proportion-

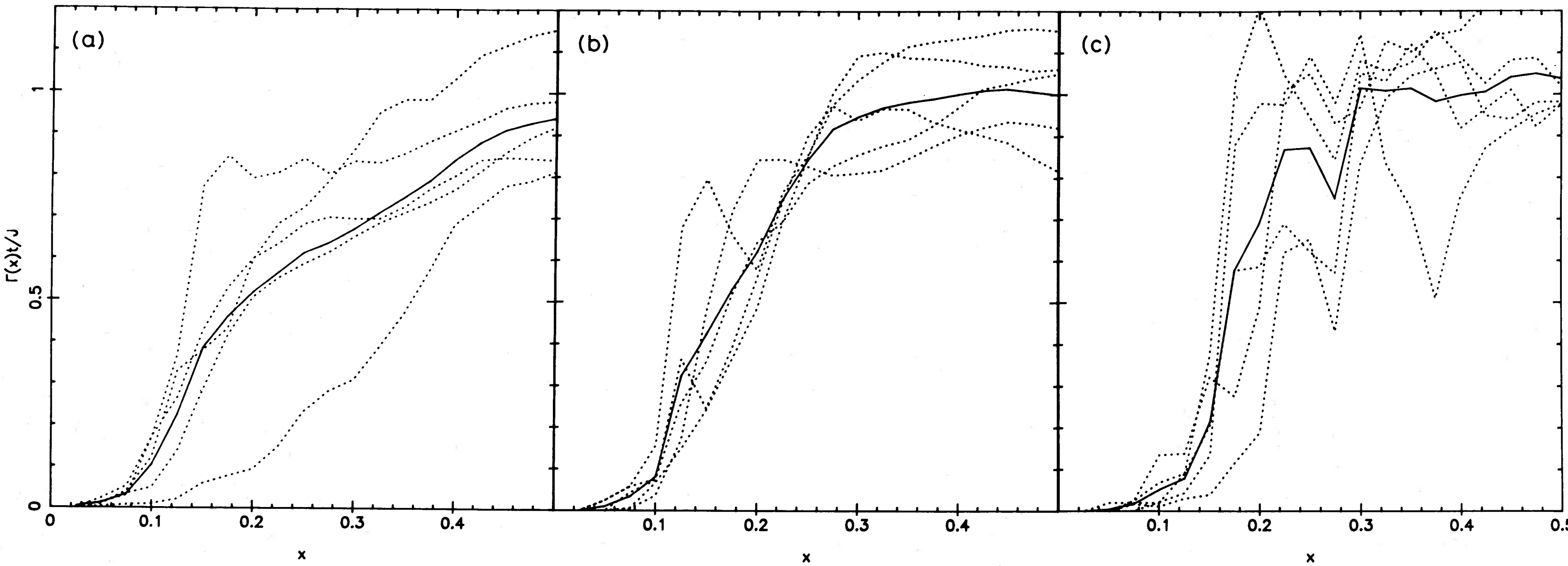

FIG. 8.—Convergence with scale of the initial torque ($a = 1$) on massive groups in our simulations. Dotted lines show the initial torque $\Gamma(x)$ from all material within radius x from the center of mass of particles which belong to massive groups. (*c*) Groups from model T0; (*b*) groups from S0; (*c*) groups from model W0. In each case, the heavy line shows the mean of the dotted lines.

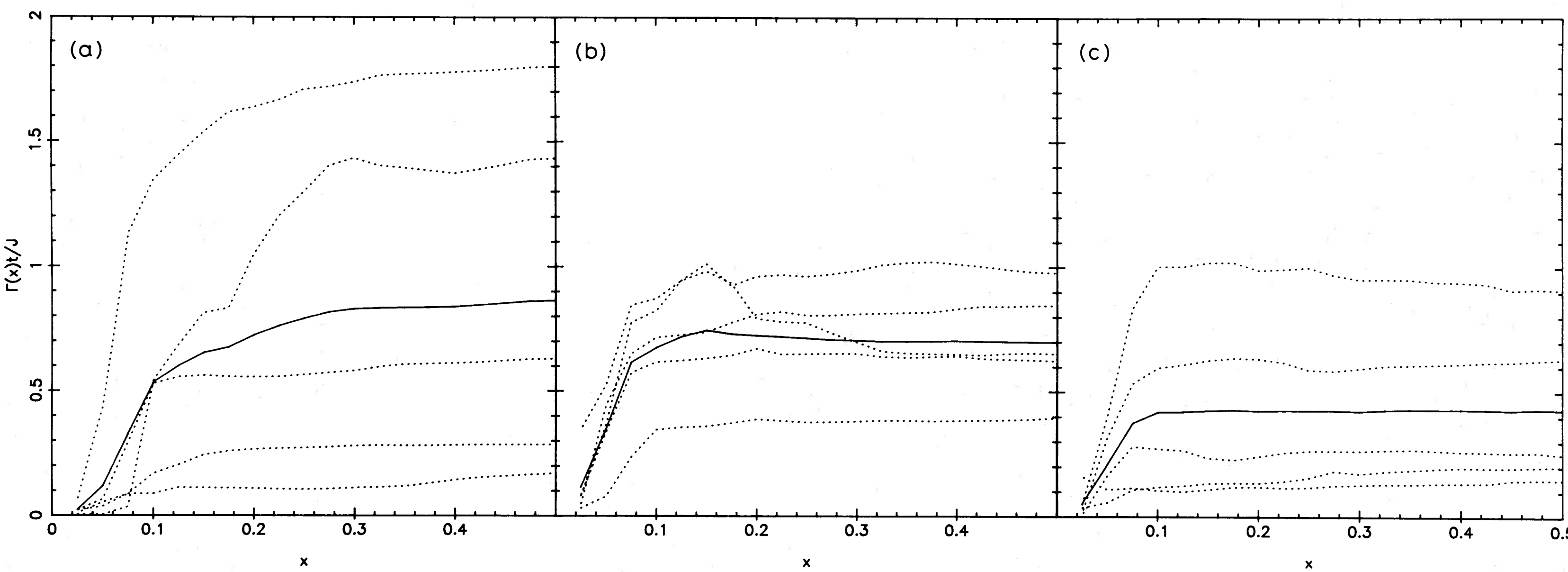

FIG. 9.—As for Fig. 8, except we have evaluated the torque on the groups at later epochs when they have become centrally concentrated. (*a*) Groups in model T0 at $a = 2.3$; (*b*) groups from S0 at $a = 3.0$; (*c*) shows groups from W0 at $a = 23.4$.

ately less important as the groups evolve. This is illustrated by Figure 9 which shows how the torques on the groups converge with increasing distance at the epochs at which the groups were identified with our group algorithm. In comparison with Figure 8, the torques shown in Figure 9 converge at a much smaller comoving radius. In particular, notice that for model T0 the main contribution to the torque on the groups at $a = 2.3$ comes primarily from material within $x \approx 0.1$, where, as described above, the initial torque converges slowly with distance.

IV. STATISTICAL PROPERTIES

Examination of massive groups has shown in some detail how angular momentum is generated and transported in individual objects. From these results it appears that tests of tidal torques based on individual objects, e.g. the Local Group (Gott and Thuan 1978) are unlikely to yield convincing results without knowledge of the distribution and kinematic properties of the dark material. If the rotation of individual objects is difficult to predict, we may still hope to find *statistical* evidence for tidal torques from the rotational properties of large numbers of objects. In this section we investigate statistical distributions and correlations of the group parameters defined in § II. In § IV*a* we study the λ distributions of our various ensembles and compare the results to previous work. In §§ IV*b*–*d* we present a systematic study of correlations among group parameters; we postpone a detailed discussion of these empirical results until § V. Finally, in § IV*e* we assess the range of validity of linear perturbation theory in predicting angular momentum growth.

a) Distribution of Group Parameters

The multiplicity function (Gott, Turner, and Aarseth 1980) is useful in characterizing the distribution of group masses. We bin groups in unit intervals of $\lfloor \log_2 M \rfloor$, so that singlets, binaries, and triples, groups of 4–7, 8–15, etc., fall in distinct bins. Each group is counted with weight proportional to its mass, so the value of each bin is the fraction of all particles in groups of the corresponding mass range. Figure 10 compares the multiplicity functions for groups, identified at a density contrast $\rho_{\rm crit} = 64\bar{\rho}$, in CDM ensembles C0–4 and S0–4 at $a = 3.0$ and white-noise ensemble W0–1 at $a = 23.4$, respectively. At these epochs, clusters of comparable mass have developed in all three ensembles, with slightly more massive objects found in the latter two. These three group catalogs will be used as our "standards."

To obtain reliable group parameters, we have imposed a lower limit to the masses of the groups. This limit was set by comparing group catalogs in models S0 and S0′. These models were generated using identical sequences of random numbers to perturb the initial grid of particles, so that they represent the same primordial density field. Model S0 has $N = 32{,}768$ particles, while in model S0′ the same density field was realized with only $N = 8000$ particles. We found a poor correspondence of properties (e.g., λ) for groups represented by less than 16 particles in model S0′. With so few particles per group, the local averaging procedure employed in the group algorithm may include particles from regions below the desired critical overdensity. A single outlying particle may contain a significant fraction of the total angular momentum of a small group. The angular momentum estimate for such groups is thus sensitive to exactly which particles are included. We emphasize that these uncertainties arise entirely from difficulties in relating a

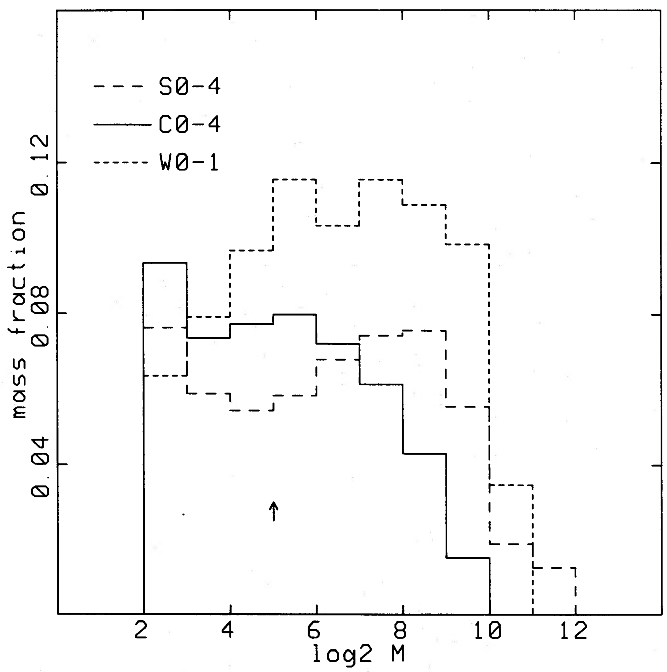

FIG. 10.—Multiplicity functions for groups identified at $64\bar{\rho}$ in the standard CDM and white-noise ensembles. The value plotted for each bin is proportional to the total mass of groups in that mass bin. Note that the cutoff $n_{\rm sph} = 4$ excludes objects in the lowest mass bins. Solid line shows results for groups in ensemble C0–4 at $a = 3.0$; some $\sim 48\%$ of the total mass is in objects of less than $n_{\rm sph} = 4$ particles. Long-dashed line gives the multiplicity function for ensemble S0–2 at $a = 3.0$; $\sim 45\%$ is in the field. Short-dashed line shows results for ensemble W0–1 at $a = 23.4$; in this case only $\sim 18\%$ is in the field. Arrow indicates the minimum mass $m_{\rm min} = 32$ of groups used in the subsequent analysis.

discrete set of particles to a smooth density field. For groups of more than 32 particles in S0′ we find good agreement between the two simulations. We have therefore restricted all of remaining analysis to objects containing $n_{\rm min} = 32$ or more particles. This should guarantee that our main results are not sensitive to the exact definitions of the groups.

The distributions of λ values in our three standard catalogs are compared in Figure 11. Despite substantial differences in the initial fluctuation spectra, the resulting λ distributions are remarkably similar. Median λ values ($\lambda_{\rm me}$) of 0.043 and 0.048 are found for CDM ensembles C0–4 and S0–4, respectively. This difference is only of marginal significance given the large variations in $\lambda_{\rm me}$ from run to run in the CDM models. For the white-noise ensemble we find $\lambda_{\rm me} = 0.052$. This is somewhat less than the value of $\lambda_{\rm me} = 0.065$ obtained by EB for model PR1, using an algorithm which identified spherical groups with an average density contrast of ~ 7. When analyzed with our new group algorithm at $\rho_{\rm crit} = 64\bar{\rho}$, model PR1 gives $\lambda_{\rm me} = 0.052$, in agreement with ensemble W0–1.

Table 4 lists values of $\lambda_{\rm me}$ derived for various ensembles and group catalogs. In general, $\lambda_{\rm me}$ is a slowly decreasing function of the critical density $\rho_{\rm crit}$ used to identify groups. This reflects the internal distribution of angular momentum within a group: much of the total J is carried by particles near the edge (§ III*b*), which are excluded as $\rho_{\rm crit}$ increases. However, λ is relatively insensitive to $\rho_{\rm crit}$ because the change in J when outlying particles are included is largely cancelled by the corresponding changes in E and M.

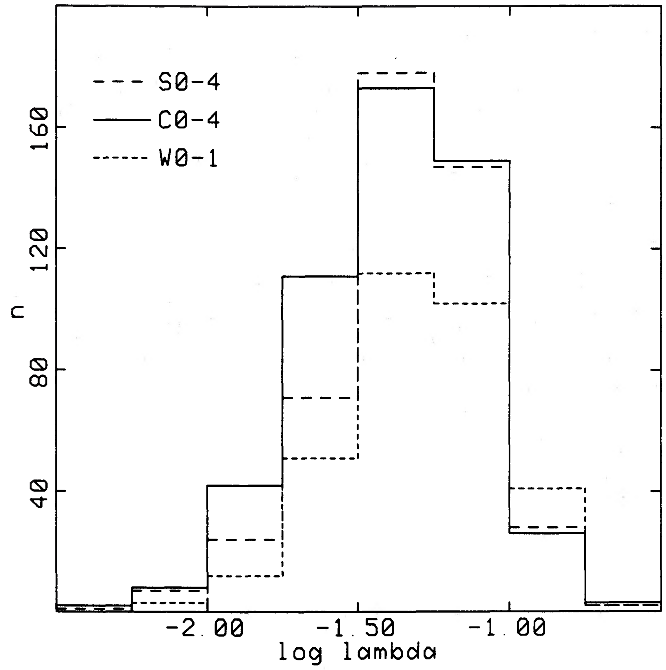

FIG. 11.—Histograms of λ; different line types denote the same group catalogs as were shown in Fig. 10

TABLE 4

PARAMETERS FOR VARIOUS GROUPS CATALOG

Models	a	ρ_{crit}	n_{min}	N_{groups}	λ_{me}
T0	2.3	64	32	55	0.047
C0–4	2.4	64	32	414	0.044
C0–4	3.0	8	32	607	0.055
		64	32	514	0.043
		512	32	264	0.037
S0–4	2.0	64	32	371	0.046
S0–4	2.4	64	32	433	0.046
	2.4	512	32	211	0.037
S0–4	3.0	64	32	459	0.048
	3.0	512	32	297	0.039
S0′	3.0	64	8	112	0.058
S0″	6.0	64	32	92	0.042
W0–1	3.88	64	8	1311	0.045
	9.54	64	16	818	0.052
W0–1	23.4	8	32	324	0.058
		64	32	324	0.052
		512	32	287	0.045

NOTES.—Scale factor of the models is denoted by a (normalized to unity at the start of a calculation), corresponding to the epoch at which the group catalogs were constructed. The resulting groups are approximately bounded by surfaces of constant density ρ_{crit} given in units of the mean density $\bar{\rho}$. We imposed a requirement of a minimum number of n_{min} particles per group; N_{group} is the total number of groups in the resulting catalog; λ_{me} is the median value of the spin parameter λ.

b) Correlations between Group Parameters

We begin by asking if tidal torques produce any significant correlation in proto-galactic mass and angular momentum content (e.g., Davies *et al.* 1983; Lake 1983). Figure 12 shows λ plotted versus group mass M for CDM ensemble C0–4 at $a = 3.0$ and white-noise ensemble W0–1 at $a = 23.4$. Open symbols show local median values of λ. For the CDM ensemble (Fig. 12*a*), a least-squares fit to the open circles gives a slope of $\beta \equiv d(\log \lambda)/d(\log M) = -0.17 \pm 0.07$, indicating a weak but detectable anticorrelation between λ and M. For the white-noise ensemble (Fig. 12*b*), local median values of λ for $a = 9.54$ and 3.88 are plotted as crosses and boxes, respectively. In plotting results from these earlier epochs, we have assumed that the λ distribution is temporally self-similar (see, e.g., Davis and Peebles 1977), so that

$$\lambda_{me}(M, t) = \lambda_{me}(M/M^*) , \qquad M^* \propto t^{4/(3+n)} , \tag{12}$$

where M^* is a characteristic clustering mass at time t (see also

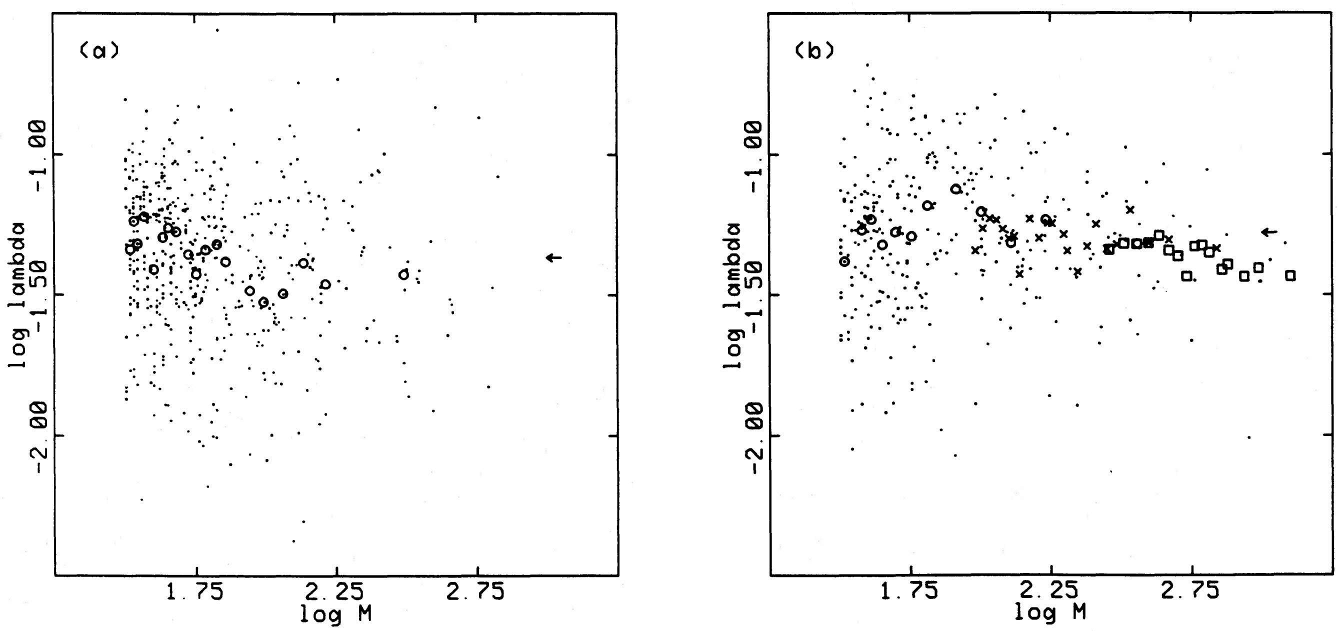

FIG. 12.—Scatter plots for spin parameter λ vs. mass M for objects identified at $64\bar{\rho}$ in CDM ensemble C0–4 when $a = 3.0$ and white-noise ensemble W0–1 when $a = 23.4$. Open circles show local median values of λ; crosses and boxes in (*b*) show medians for $a = 9.54$ and 3.88, respectively, scaled according to the self-similarity relation eq. (12).

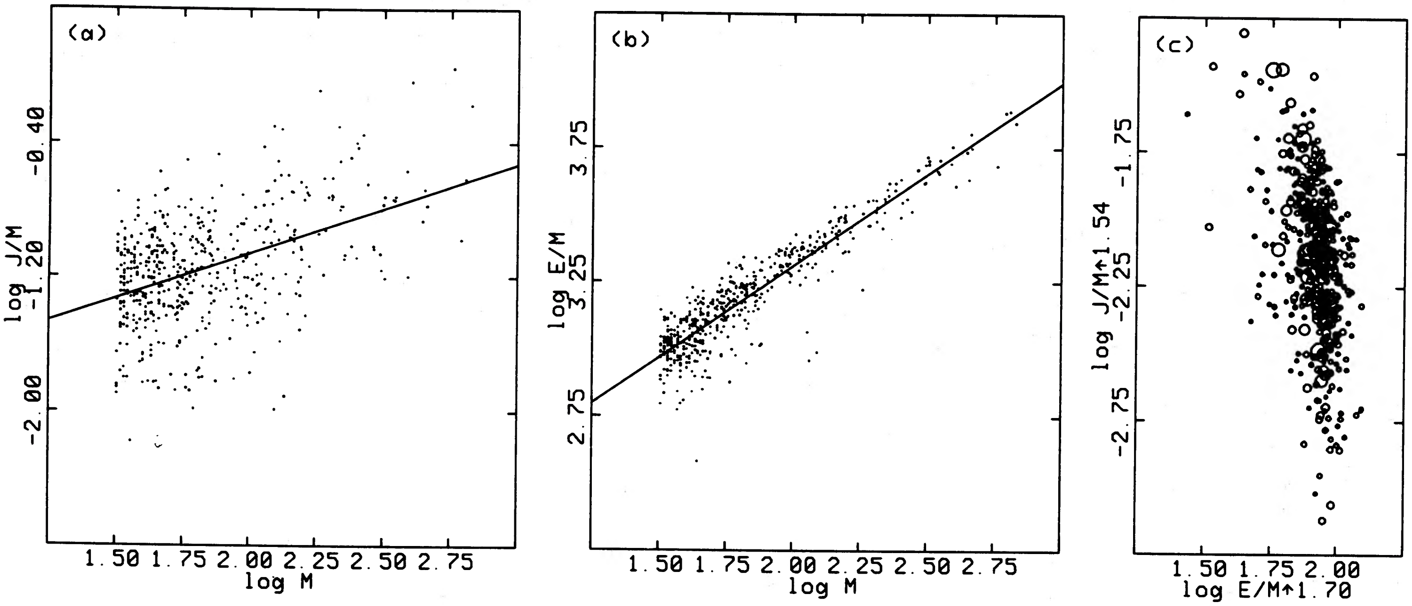

FIG. 13.—Specific angular momentum j and binding energy ϵ plotted vs. group mass M for CDM ensemble C0–4. Straight lines are the power-law fits given in eq. (13). (c) Residuals from the j-M and ϵ-M power laws vs. each other. Objects are plotted as circles with area proportional to M.

EB). Thus, the masses of objects from $a = 9.54$ and 3.88 were multiplied by factors of $(23.4/9.54)^2 = 6$ and $(23.4/3.88)^2 = 36$, respectively. Although individual medians (each computed from ~ 24 or more groups) scatter considerably, the general continuity between the three epochs suggests that the λ distribution is indeed self-similar. A least-squares fit to the entire set of medians gives $\beta = -0.08$.

To get some idea of why the λ distribution is so broad, we have examined the specific angular momenta $j \equiv J/M$ and binding energies $\epsilon \equiv E/M$ of the groups. In Figure 13a–13b we plot j and ϵ against mass for objects in CDM models. Both parameters correlate strongly with M; least-squares fits given the following relations:

$$j \propto M^{\tau}, \quad \tau = \begin{cases} 0.54 \pm 0.05, & \text{C0–4}, \\ 0.70 \pm 0.05, & \text{W0–1}, \end{cases} \tag{13a}$$

$$\epsilon \propto M^{\kappa}, \quad \kappa = \begin{cases} 0.69 \pm 0.01, & \text{C0–4}, \\ 0.56 \pm 0.01, & \text{W0–1}. \end{cases} \tag{13b}$$

The regressions show small but significant differences between the white-noise and CDM models. These relations, together with the definition of λ, lead to $\lambda \propto M^{\tau+\kappa/2-1}$; although the relations in equation (13) depend on spectral index, the combination $\tau + \kappa/2 - 1$ is nearly independent of the power spectrum, and numerically close to the measured value of β. For both sets of models, the scatter in the j-M relation is much larger than that in the ϵ-M relation. This is shown in Figure 13c where we have plotted j/M^{τ} against ϵ/M^{κ}, eliminating the variance contributed by M. Most of the groups fall in a highly elongated ellipse nearly aligned with j/M^{τ}; only a small part of the variance in j is due to the variance in ϵ. Although a weak anticorrelation of j and ϵ is indicated, it is clear that binding energy is a poor predictor of angular momentum. This argues against the results of Hoffmann (1986), who suggested that tightly bound groups would collapse before acquiring much angular momentum. Our analysis shows that almost all of the scatter in λ arises from scatter in j/M^{τ}. To try to understand what factors determine λ, we study several other correlations.

Figure 14 shows scatter-plots of λ versus substructure, as measured by f_2/f_1. This ratio is small for monolithic centrally condensed objects and close to unity for binaries with comparable components. We find a significant tendency for objects with little substructure to have low λ-values compared to the overall distribution; this is more apparent in the CDM models, in part because the higher part of the f_2/f_1 range is better populated. Such an effect is expected in the tidal torque picture because binaries, which typically have large quadrupole moments, are strongly coupled to the tidal field. A similar correlation is found between λ and the major- to minor-axis ratio a/c, which is related to quadrupole moment by equation (5).

In § IIIc we showed that the main contribution to the torque on a typical group in our simulations arises from nearby material. We might then expect those objects with nearby neighbors to be subject to stronger tidal fields and therefore have higher λ. It is not clear, however, that this should be a strong effect, since the torque also depends on the orientation of the quadrupole moment with respect to the separation vector to the nearest neighbor. We test for this effect in Figure 15, where we plot λ of each object versus nearest neighbor distance x_{nn} for ensembles C0–4 and W0–1. As expected, high λ objects do tend to have nearer neighbors, but this effect is always quite weak. The large scatter in these plots is not significantly reduced if instead of x_{nn} we plot the tidal field due to the nearest neighbor, which scales as $m_{nn} x_{nn}^{-3}$.

The possible implications of a correlation between overdensity and protogalactic angular momentum of the origin of the Hubble sequence have been alluded to in the introduction. In Figure 16, we show correlations of λ with mean initial overdensity $\langle \nu \rangle$, computed using a smoothing length of $x_s = 1/64$. Results for the CDM ensemble are plotted in Figure 16a; although a strong correlation between $\langle \nu \rangle$ and mass M (proportional to circle area) is apparent, there is only marginal

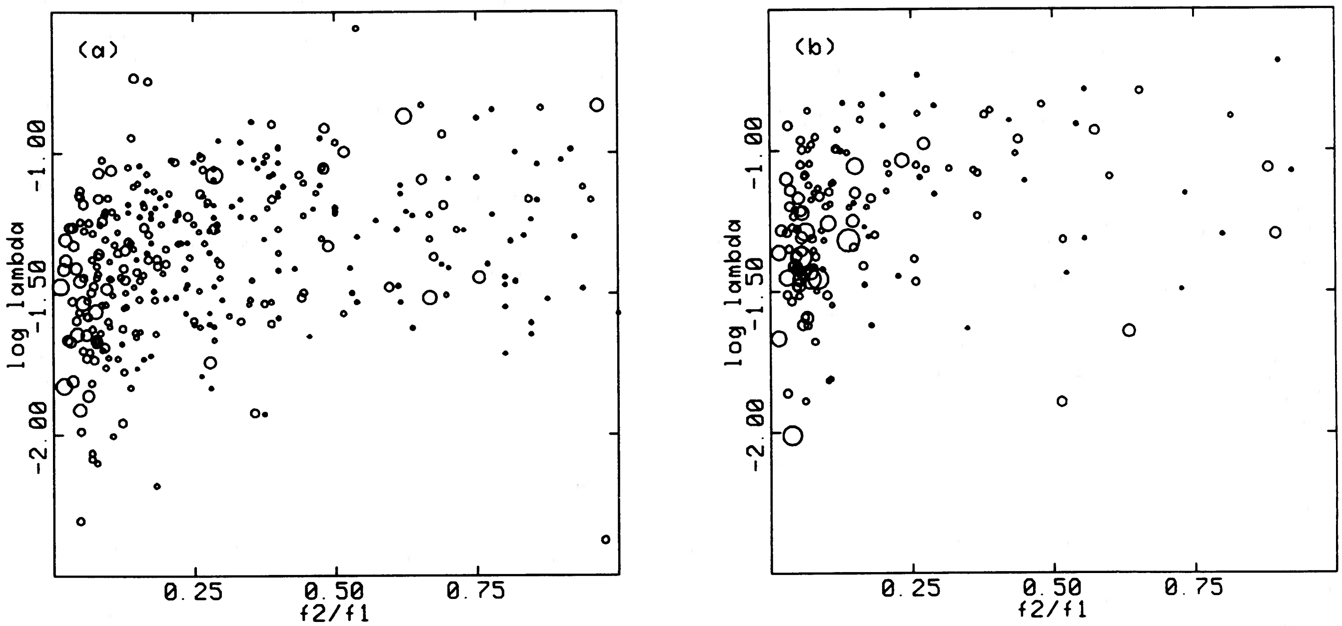

FIG. 14.—Scatter plots for spin parameter λ vs. substructure index f_2/f_1, which measures the "binaryness" of an object, for the ensembles used in Fig. 12

evidence for a trend of λ with $\langle v \rangle$. A weak anticorrelation of λ and $\langle v \rangle$ could be induced by the observed correlations between λ and M and between M and $\langle v \rangle$. Results for the white-noise models are plotted in Figure 16*b*; no trend is found at this epoch or at earlier ones (which yield a broader $\langle v \rangle$ distribution). Similar null results are found for other values of x_s. At face value, these results directly conflict with the suggestion that angular momentum is strongly anticorrelated with initial overdensity (Blumenthal *et al.* 1984). There are several possible criticisms of our analysis. First, the smoothing length x_s is an unphysical parameter which cannot readily be identified with the characteristic sizes of groups. Nevertheless, as we show in Figure 2, the particles at high v do succeed in tracing the dense spots where rich groups form. Second, we would have difficulty detecting an anticorrelation of λ and v if it only set in, e.g., for $v > 2.0$, since our N-body simulations contain few objects with such high overdensities. However, as we will show in the next section, the spatial distribution of objects with different λ does not conform to the predictions of Blumenthal *et al.* In addition, we show directly in § IV*e* that linear theory calculations of J yield poor estimates of the angular momentum of objects which have detached from the Hubble flow.

c) Spatial Distribution

We next ask more generally if a picture of galaxy formation linking λ and galactic morphology can account for the

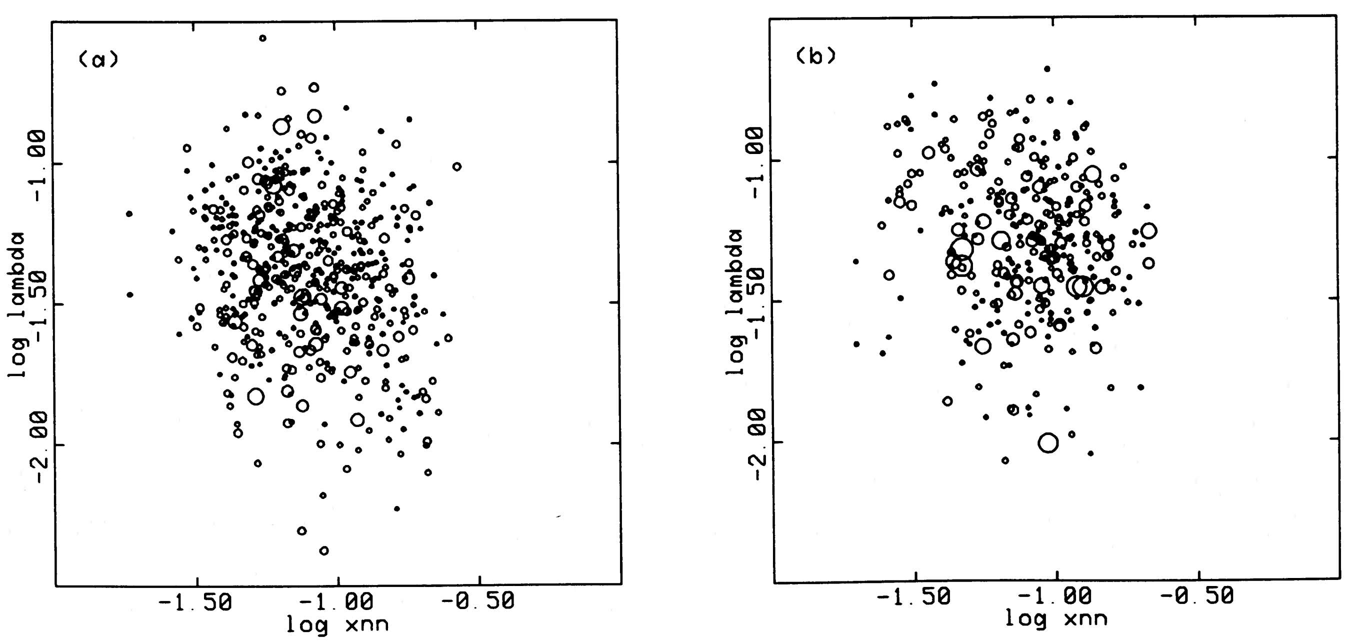

FIG. 15.—Scatter plots of spin parameter λ vs. nearest neighbor distance x_{nn} for the ensembles used in Fig. 12

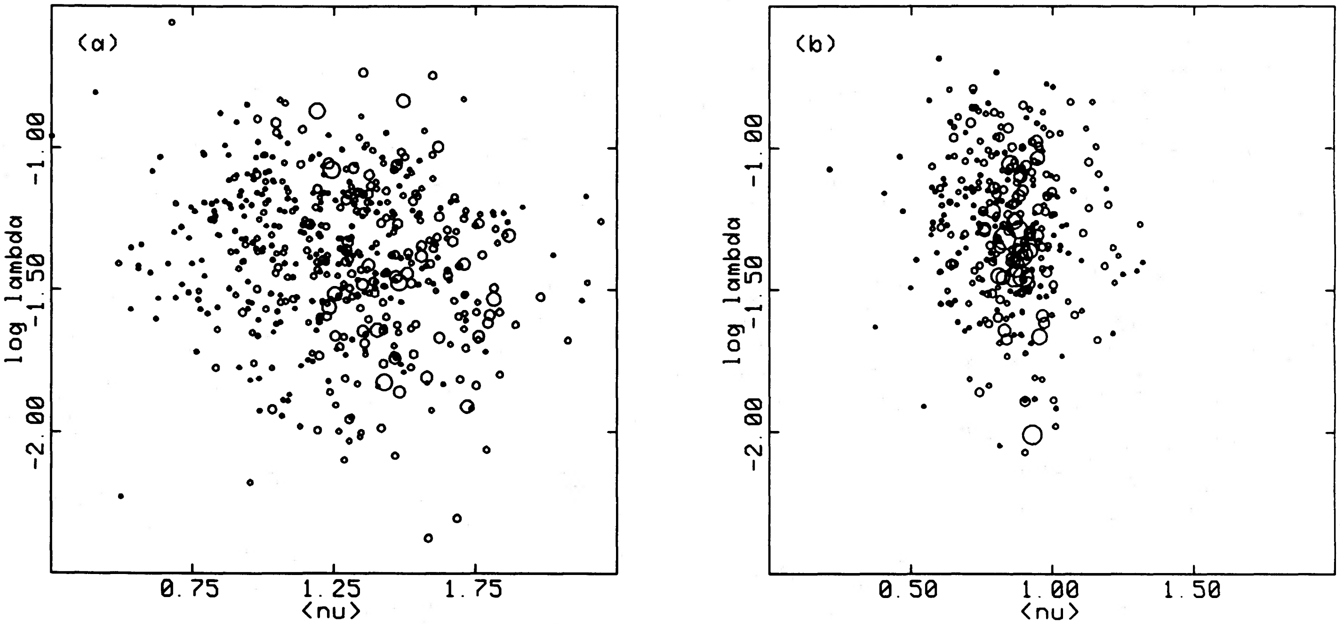

FIG. 16.—Scatter plot of spin parameter λ vs. initial overdensity $\langle \nu \rangle$. No effect is seen, although a trend between mass M and $\langle \nu \rangle$ is apparent in the CDM data.

observed relation between type and environment. Specifically, we compare the autocorrelation functions $\xi_>$ and $\xi_<$ for separate catalogs of groups with λ values above and below the median $\lambda_{\rm me}$. A large difference in the spatial distributions of rapidly versus slowly rotating groups might then be expected to induce a corresponding difference in the spatial distributions of different types, which could be compared to the observations.

In Figure 17 we present representative results for ensembles C0–4 and W0–1; in addition to $\xi_>$ and $\xi_<$, we plot the mass correlation function ξ_ρ. One sigma error bars were estimated by comparing results for different models in each ensemble. We find that high λ objects are *more* clustered than those with low λ. In ensemble C0–4, which shows the strongest effect, $\xi_>$ and $\xi_<$ have similar slopes but the amplitude of ξ for the high λ objects is a factor of ~ 2.5 above that for low λ objects. The size of this effect depends on $\rho_{\rm crit}$ and $n_{\rm min}$, which together determine the rarity of the objects in our catalogs; qualitatively we find that the effect is stronger in group catalogs containing only massive, rare objects. A correlation between λ and clus-

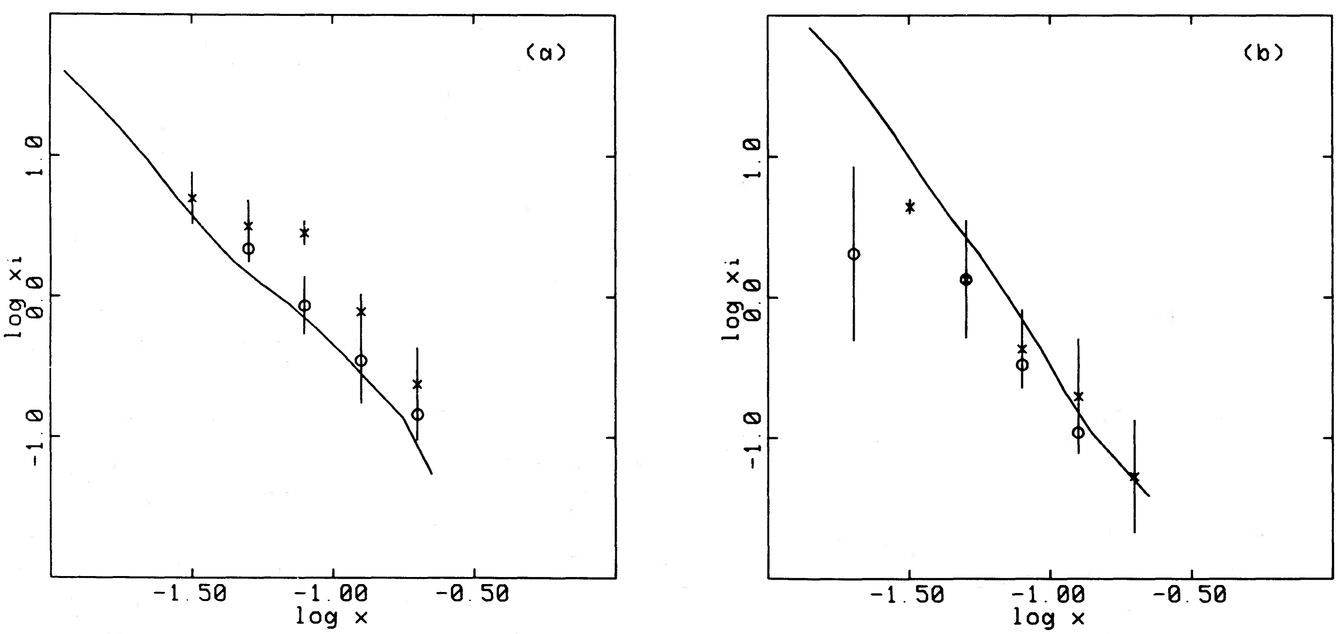

FIG. 17.—Two point correlation functions for rapidly and slowly rotating groups in ensembles (*a*) C0–4 and (*b*) W0–1. Results for disjoint catalogs of groups with λ values above and below the ensemble $\lambda_{\rm me}$ are plotted as circles and crosses, respectively; error bars are estimated from the variation from one model to another in each ensemble. Solid curves show the correlation functions of the underlying mass distribution.

tering is physically reasonable, since those objects which are highly clustered should be subject to stronger tidal fields, consistent with our results for λ and nearest neighbor distance x_{nn}. Our result is in agreement with the qualitative argument presented by Bardeen *et al.* (1986, § V*b*). Note, however, that the sign of the effect is *inconsistent* with the idea that low λ objects become elliptical galaxies; if λ were the sole determinant of gross galactic morphology, we would expect spirals to be slightly more clustered than ellipticals, in contradiction with observation.

d) *Alignment Statistics*

The idea that tidal torques might produce significant alignments in the rotation axes of adjacent galaxies has generated both theoretical and observational work (e.g., Hawley and Peebles 1975; Jones 1976; Sharp, Lin, and White 1979; Helou 1984). In this section some of the proposed "signatures" of tidal torques are checked against the N-body simulations.

A single object defines two directions: the spin vector $\boldsymbol{J}$ and the (bidirectional) major-axis vector $\boldsymbol{A}$. We begin by looking at the internal alignment of these directions. Figure 18 is a histogram of $|\hat{\boldsymbol{J}}_i \cdot \hat{\boldsymbol{A}}_i|$, the cosine of the angle between the spin- and major-axes of object i. The solid line is data for all objects in ensemble C0–4, while the dashed line is for a subset with less substructure, $f_2 < f_1/4$. If $\boldsymbol{J}$ and $\boldsymbol{A}$ were independent, these data would be uniformly distributed. The histograms show that the spin- and major-axes of objects tend to be perpendicular; a similar trend is found in other catalogs. This effect is, of course, consistent with the standard tidal torque picture, but would also appear if $\boldsymbol{J}$ and $\boldsymbol{A}$ were both determined by a single outlying subobject with a large transverse motion. The low-substructure subset provides a simple test of this possibility; the alignment is nearly as strong in the subset, so we conclude that substructure does not dominate the measured effect.

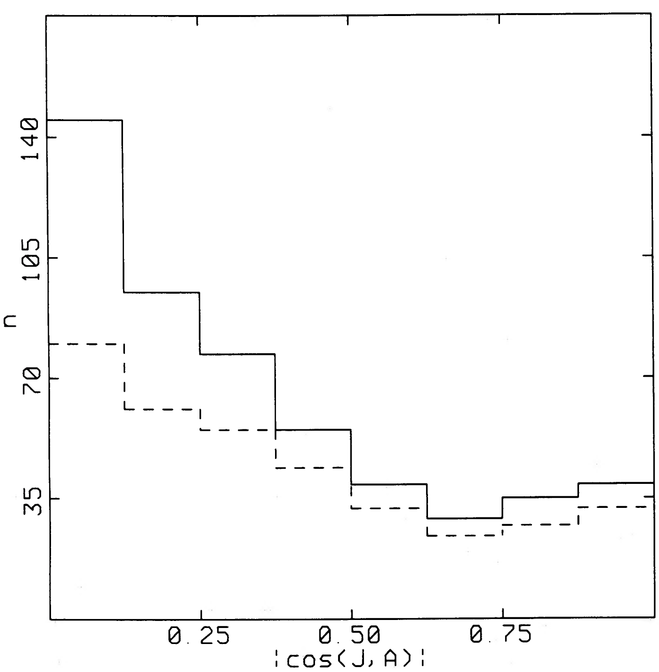

FIG. 18.—Test for alignment between the spin $\boldsymbol{J}$ and major axis $\boldsymbol{A}$ of objects identified at $64\bar{\rho}$ in ensemble C0–4 when $a = 3.0$. Histograms show the distribution of $|\hat{\boldsymbol{J}} \cdot \hat{\boldsymbol{A}}|$, the cosine of the angle between $\boldsymbol{J}$ and $\boldsymbol{A}$; random orientations would produce a uniform distribution. Dashed line is from a subset of objects selected to have less substructure, $f_2 < f_1/4$.

A pair of objects in turn define five directions: two spin vectors, two major-axes, and one separation vector. With these we could, in principle, generate a large number of statistical alignment tests (some of which, by chance, could appear "significant"). Instead, we focus on tests for *alignment* between a direction defined by an object and the separation vector toward a nearby object, and tests for *coherence* in a direction field defined by a field of objects. All of these tests involve collecting statistics for a restricted subset of the set of all pairs of objects (i, j) in each simulation; after considering a number of ways of defining such subsets, we focus on the subsets of all pairs within comoving distance x_{sep} of each other, for various values of x_{sep}.

1. In all of our ensembles we find that nearby objects "tend to point toward each other," i.e., for nearby i and j, $\boldsymbol{A}_i$ tends to be parallel to the separation vector $\boldsymbol{x}_{ij}$ (parallel and antiparallel are not distinguished). This is shown in Figure 19*a*, where we plot histograms of $|\hat{\boldsymbol{A}}_i \cdot \hat{\boldsymbol{x}}_{ij}|$ for the standard ensembles. Results are shown for all pairs within $x_{sep} = 0.10$ (lower set of histograms) and 0.16 (upper set). If the vectors were uncorrelated, the expected distribution would be uniform. A correlation was reported in observations of Abell clusters by Binggeli (1982) and studied in N-body simulations with white-noise, adiabatic, and "mixed" spectra by Dekel, West, and Aarseth (1984). They found this effect to be significant in the latter two cases but not in the white-noise models; however, the weak effect shown by the dotted lines in Figure 19*a* may have been undetectable in their smaller data set.

2. To look for coherence in the orientation of nearby objects, Figure 19*b* shows histograms of $|\hat{\boldsymbol{A}}_i \cdot \hat{\boldsymbol{A}}_j|$, the cosine of the angle between the major-axes of objects i and j, for the same sets of pairs as in Figure 19*a*. We find a consistent tendency for nearby objects to point in the same direction in the CDM models but not in the white-noise ensemble. This effect, along with the related effect described in the last paragraph, reflect the "filamentary structure" of the CDM models (Fig. 1).

3. We now turn to discuss alignment statistics involving the spin vectors of nearby objects. In Figure 19*c*, we plot histograms of $|\hat{\boldsymbol{J}}_i \cdot \hat{\boldsymbol{x}}_{ij}|$ for pairs in the three standard ensembles. A weak tendency for $\boldsymbol{J}$ and $\boldsymbol{x}$ to be perpendicular is suggested in the results for ensembles S0–4 and W0–1. While no effect is seen in ensemble C0–4 at this particular epoch and overdensity, a weak but consistent tendency for nearby neighbors to lie in an object's spin plane is found in other CDM results. An alignment effect of this kind is expected at some level if nearest neighbors have aligned quadrupole moments.

4. Finally, we look for coherence in the spin vectors of nearlby objects. Figure 19*d* presents histograms of $\hat{\boldsymbol{J}}_i \cdot \hat{\boldsymbol{J}}_j$ for pairs selected using the same criteria as above (this is the only test in which we can sensibly distinguish between parallel and antiparallel). In general, no coherent pattern emerges: the small-box ensemble exhibits no effect at all, while in the big-box and white-noise ensembles objects appear to be weakly parallel and antiparallel, respectively. None of these trends appear reliably in group catalogs constructed at other epochs or density contrasts. Similar results were obtained for pairs (i, j) which are mutually nearest neighbors; this set includes a high proportion of physically associated pairs. We conclude that tidal torques do not produce a significant degree of coherence in the spins of nearby objects.

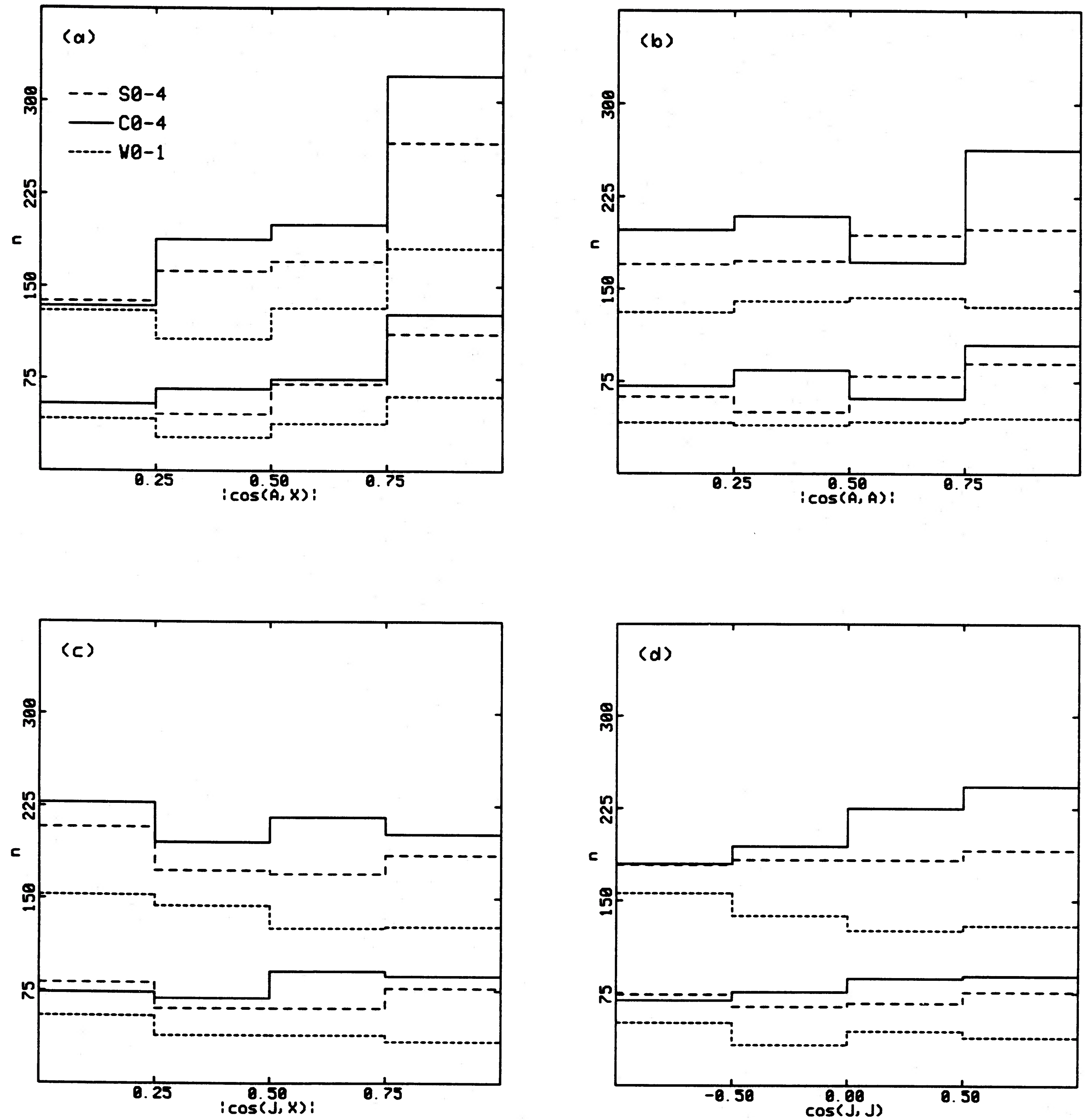

FIG. 19.—(*a*) Test for alignment between the major axes of objects and directions toward nearby neighbors, identified at $64\bar{\rho}$ in ensembles S0–4 (*dashed lines*) and C0–4 (*solid*) when $a = 3.0$ and ensemble W0–1 (*dotted*) when $a = 23.4$. Distribution of $|\hat{A}_i \cdot \hat{x}_{ij}|$ is plotted for pairs with $|x_{ij}| < x_{\rm sep}$, where $x_{\rm sep} = 0.1$ (*lower histograms*) and 0.16 (*upper*). Objects tend to point at each other in all simulations, although the effect is much stronger with CDM. (*b*) Test for coherence in the major-axis directions of nearby objects. The distribution of $|\hat{A}_i \cdot \hat{A}_j|$ is plotted for the same sets of pairs as in (*a*). A weak effect is seen in the CDM ensembles, but not in the WN. (*c*) Test for alignment between the spin vectors of objects and directions toward nearby neighbors. (*d*) Test for coherence in the spin vectors of nearby objects. Histograms of $\hat{J}_i \cdot \hat{J}_j$ are plotted for the sets of pairs used in (*a*).

e) Evolution of Angular Momentum and Applicability of Linear Theory

In § III we presented results for the evolution of angular momentum in a small number of clusters selected from our simulations and showed how nonlinear effects are important in terminating the growth and in fixing the spatial distribution of angular momentum. Similar effects can be demonstrated in a statistical fashion, without reference to the detailed evolution of individual groups.

As an example, we have analyzed our "standard" group catalogues for ensembles C0–4 and W0–1 (defined at $a = 3.0$ and $a = 23.4$, respectively, with $\rho_{\rm crit} = 64\bar{\rho}$) in the following way. We computed the binding energy of each particle with respect to all other particles belonging to the same group. The curves labeled 1–4 in Figure 20 show the evolution of the mean specific angular momentum of particles with binding energies which lie within the following percentile points of the *overall* distribution: (0%–10%), (10%–20%), (20%–50%), and (50%–100%), respectively (only objects with $n \geq 32$ particles in the most tightly bound percentile bin were used). Thus curve 1 shows the evolution of weakly bound particles, while curve 4 shows the behavior for tightly bound particles.

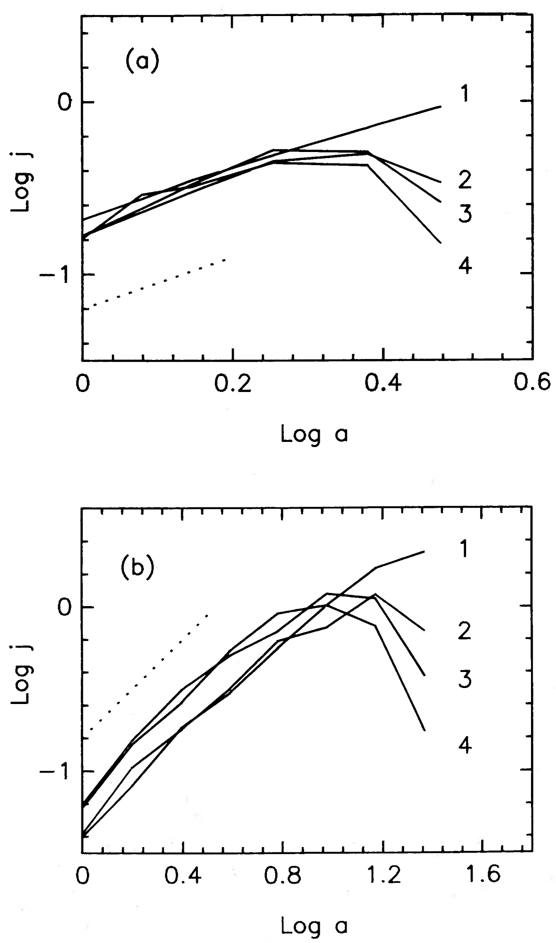

FIG. 20.—Specific angular momentum j as a function of expansion factor a for particles in various binding energy bins. The curves labeled "1" show the evolution for weakly bound group members, while the curves labeled "4" show the evolution for strongly bound members (see text in § IV*e* for details). (*a*) Results for ensemble C0–4; (*b*) results for ensemble W0–1. Dotted lines show the linear theory prediction $j(t) \propto t$.

The dotted lines show the expected linear-theory behavior (eq. [8]), which is in good agreement with the simulations at early times. As clumps becomes nonlinear, the rate of angular momentum growth falls away from the linear prediction. The subsequent decrease in specific angular momentum of the more tightly bound particles reflects the outward transport of angular momentum by nonlinear dynamical effects as outlined in § III. Notice that the most tightly bound particles begin to loose angular momentum sooner than less tightly bound particles and that by the final times shown in Figure 20, the mean specific angular momentum of the most tightly bound set of particles is about a factor of 3 lower than that for the most loosely bound set. As we have shown in § III, the difference in j between the inner and outer parts of individual clumps can be even larger than this. These results confirm our statement in § III*b* that the decay of angular momentum during the nonlinear evolution of clumps is a general feature of our numerical simulations.

We now check whether linear perturbation theory can be used to estimate even qualitatively the total angular momentum of a mildly nonlinear clump. In Figure 21*a*, we plot the final angular momentum $J_{\rm final}$ of clusters in model C4 (identified at $a = 3$ with $\rho_{\rm crit} = 64$) against the angular momentum "predicted" by linear theory $J_{\rm pred}$, which is computed by evaluating the angular momentum of group members using the initial conditions and then extrapolating to $a = 3$ using the growth rate given in equation (8). The initial conditions provide a reliable estimate of the initial angular momentum, since J accurately follows the linear theory growth rate at early times.[2] As this figure shows, there is a good correlation between $J_{\rm final}$ and $J_{\rm pred}$. However, this is merely the result of the strong correlation between J and total group mass. Large groups tend to have large angular momenta, and this trend is correctly predicted by linear theory. The quantity $J_{\rm final}$ is, on average, ~ 3 times smaller than $J_{\rm pred}$, and the total scatter about the mean relation is also a factor of ~ 3. Thus linear theory predicts the correct order of magnitude of $J_{\rm final}$, but even if we multiply $J_{\rm pred}$ by a constant factor to account qualitatively for the reduced growth of J in the nonlinear regime, the scatter in the predictions for groups of fixed mass will be comparable to the width of the distribution of λ. This is demonstrated in Figure 21*b*, which shows $J_{\rm final}/J_{\rm pred}$ plotted against λ. If linear theory were to provide a useful guide of correlations between λ and other parameters, we would expect that the distribution of points on this figure would be highly elongated in the λ direction. In fact, the elongation is relatively small, showing that nonlinear effects are important in determining the final value of λ. In Figure 21*c*, we show the analogous diagram for groups identified at a lower density contrast, $\rho_{\rm crit} = 8\bar{\rho}$. This shows a tighter correlation, as we would expect since these groups are only mildly nonlinear, but even here the scatter is substantial. Notice that in both figures the scatter in $J_{\rm final}/J_{\rm pred}$ among the larger groups is less than that of the smaller groups. Similar results are found for white-noise initial conditions (Fig. 21*d*). The only difference is that $J_{\rm final}/J_{\rm pred}$ is lower by an additional factor of ~ 3 compared with groups identified at the same density contrast in the CDM models. This is primarily because low-mass groups decouple from the Hubble flow over a wide range in time.

[2] As an additional check of the accuracy of our initial conditions, we ran model S0″, which has exactly the same set of perturbations as model S0, but with initial amplitude lower by a factor of 2. The angular momenta of corresponding groups are in good agreement even at late times.

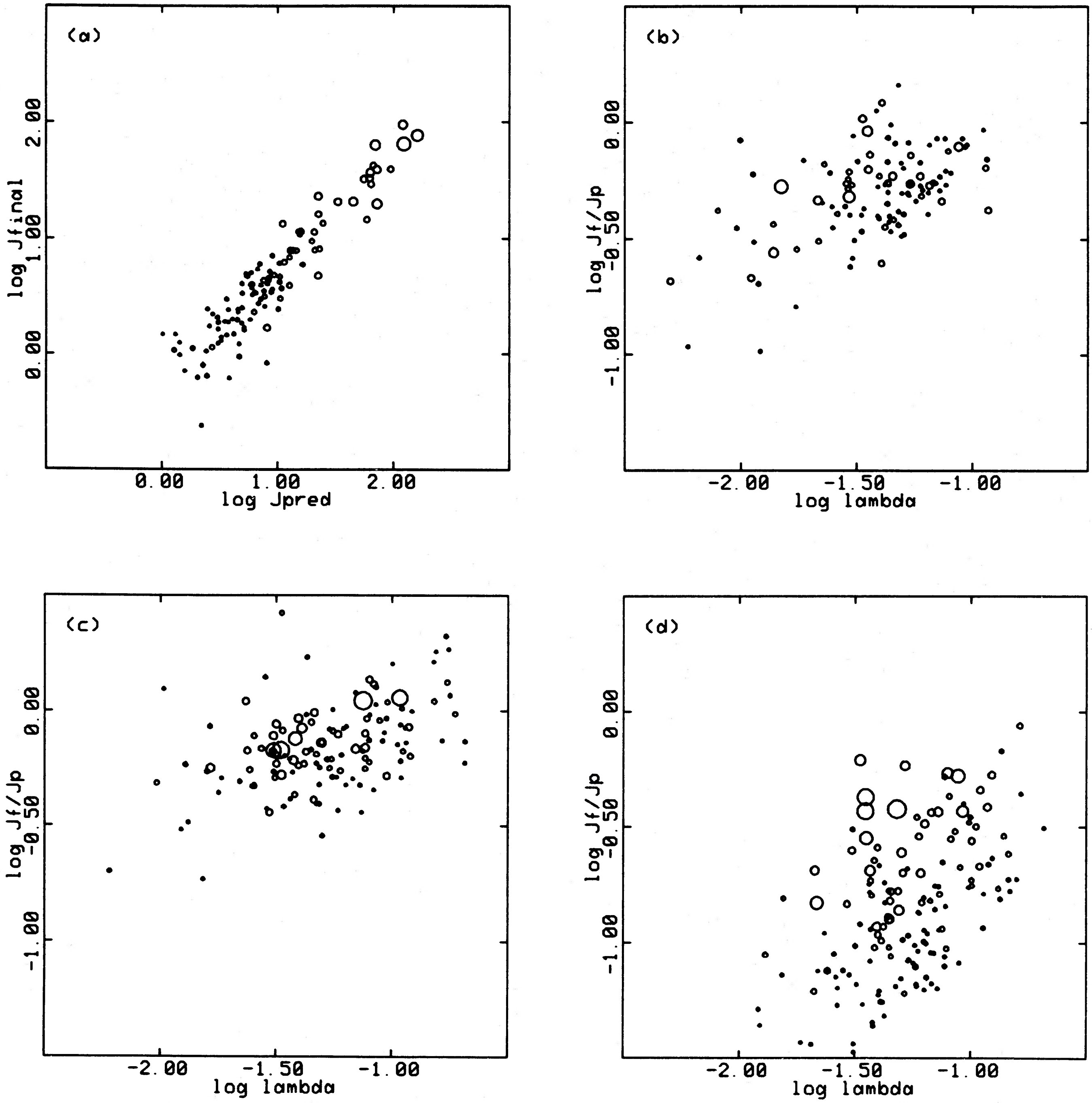

FIG. 21.—(*a*) Final angular momenta ($J_{\rm final}$) of groups in model C4 identified at $a = 3.0$ with $\rho_{\rm crit} = 64\bar{\rho}$ plotted against predictions of linear theory $J_{\rm pred} = J(t_i)a^{3/2}$. Circle area is proportional to mass M. (*b*) Plot of $J_{\rm final}/J_{\rm pred}$ against λ for the groups in model C4 used to construct (*a*). (*c*) Equivalent plot for groups identified at a lower density contrast ($\rho_{\rm crit} = 8\bar{\rho}$) at $a = 3.04$ in model C4. (*d*) Results for groups identified at $a = 23.4$ with $\rho_{\rm crit} = 64\bar{\rho}$ in model W0.

These results demonstrate clearly that angular momenta of clumps with even modest overdensities are altered by nonlinear effects. The physical mechanisms involved can be roughly grouped into two categories. First, as groups become nonlinear, the angular momentum grows more slowly than predicted by equation (8). This is because the clumps become more centrally concentrated as they evolve and therefore become more weakly coupled to the tidal field (§ III*b*). This sort of "saturation" effect was anticipated by Peebles (1969) in his calculation. Second, angular momentum is transported from the inner parts of groups to their outer parts by gravitational torques. This effect is more pronounced at high-density contrasts. The results in Figure 21 show that linear theory can provide, at best, only a rough guide to the angular momenta of nonlinear groups. Since we have shown in previous sections that λ is only weakly correlated with other group parameters, it is quite likely that arguments based on linear theory could lead to misleading conclusions and spurious correlations.

Some implications of these nonlinear effects for models of galaxy formation will be discussed in § V.

V. CONCLUSIONS

We have studied the growth and distribution of angular momentum in bound objects formed by gravitational clustering in large cosmological N-body simulations. Initial conditions for our simulations range from white noise ($n = 0$) to the kind of spectra predicted on the scales of galaxies and groups in a biased $\Omega = 1$ CDM cosmogony ($n_{\rm eff} \approx -2.2$).

Our analysis of individual massive groups has led to the following results. The groups are centrally concentrated with "circular" velocity profiles $v_c(x) = [GM(x)/x]^{1/2}$, which are nearly flat in the CDM–like models ($n_{\rm eff} \approx -2$) and decline slowly ($\propto x^{-0.25}$) for white-noise models. These results are compatible with those of Frenk *et al.* (1985) and Quinn, Salmon, and Zurek (1986). The specific angular momentum for material near the center of a group is lower than that for material in the outer parts. This behavior is well approximated by the relation $j(x) \propto x$ and is independent of initial conditions. While groups represent small density perturbations, their angular momentum grows as $J(t) \propto t$, in accord with the predictions of linear theory. As groups become nonlinear, their angular momentum at first grows more slowly and then decreases at later times. The loss of angular momentum arises primarily from the orbital angular momentum associated with subclumps which is transferred to external material as they fall toward the center of a group and merge. This process plays an important role in determining the spatial distribution of angular momentum in the central, high-density regions of groups. The direction of the spin vector for high-density material ($\Delta > 500$) is often poorly correlated with that for material in the outer parts of groups.

We find that the overall distribution of the dimensionless spin parameter λ in our models is broad and shows no significant trend with spectral index. A weak tendency for massive objects to have lower λ values is seen in both CDM and white-noise models. A more striking correlation is found between λ and substructure, especially in the CDM models; this correlation reflects the better coupling of binaries to the tidal field. However, we find only a weak indication that λ is correlated with nearest neighbor distance in the sense generally expected from tidal torques, and no significant correlation between λ and initial overdensity as measured by $\langle \nu \rangle$. In CDM–like models, the more rapidly rotating objects (with $\lambda > \lambda_{\rm me}$) are somewhat more clustered than slowly rotating ones. The white-noise models do not show any significant correlation of this kind.

At first sight some of these trends may appear contradictory. For example, in the CDM models groups with high mass tend to have high ν and to cluster more strongly than low-mass groups, yet we find that high-mass groups tend to have low λ values and groups with high λ cluster more strongly than those with low λ. Apparent contradictions of this kind are common in complex multivariate problems (see, e.g., Kendall 1975). The λ distribution is broad and may be weakly correlated with several parameters. When we plot scatter diagrams, we project the distribution of points in the hyperspace of group parameters onto several different planes. Weak correlations in two such planes *cannot* generally be combined to interfer a correlation in any other. We feel that this is an important point, since it shows that future analytic treatments of angular momentum in protogalaxies will have to consider several variables before they can make reliable predictions.

We find that the spin- and major-axes of typical objects tend to be perpendicular, although a wide range of shapes and spin orientations are found. Nearby objects tend to point at each other in both CDM and white-noise models, and the major axes of CDM groups appear to define a coherent direction field. Spin-vector directions, on the other hand, are much less orderly. We find only a weak indication that objects tend to spin at right angles to nearby neighbors, and no consistent indication of coherence in the spins of adjacent objects; the tidal torque mechanism produces no significant (i.e., easily detectable) spin orientation effects. Some insight into this result may be provided by the following. The most striking effect seen in these tests is the tendency for nearby objects to point at each other. It seems likely that objects are "born" with these orientations; if they had been formed with random major axes and sheared into line by tidal torques, we would expect a strong spin-vector versus separation-vector effect, which we do not find. This point is also supported by direct inspection of plots such as Figure 1. As Binney and Silk (1979) observed, an object which is born with its major axis already pointing at a nearest neighbor receives no torque from that neighbor; it can only be spun up by the tidal field of more distant objects. This alignment may account for the weakness of the λ versus nearest-neighbor correlation (§ IV*b*). A weak spin separation effect could arise solely from the strong tendency of objects to have perpendicular spin and major axes and major axes pointing at nearby objects.

The lack of spin alignment seen in our simulations is consistent with observational studies which have found no evidence of significant alignment between galaxies which are nearby neighbors (Hawley and Peebles 1975) or members of a binary (Sharp, Lin, and White 1979). Recently, Helou (1984) has used 21 cm data and other clues (e.g., spiral structure) to disentangle the projected spin-vector orientations of 31 relatively isolated pairs of galaxies. He finds what appears to be a significant tendency for the spin vectors to be antiparallel. Any effect of this magnitude would be easy to detect in our simulations. Indeed, it is hard to see how tidal torques could produce an effect of the kind reported by Helou. Conservation of angular momentum does not imply antiparallel spins: an isolated pair of galaxies born with suitable orientations could spin in the same direction and orbit around each other in the opposite direction. If Helou's conclusions are correct, they will have a major impact on our understanding of the origin of galactic angular momentum. It is therefore urgent that a similar analysis be performed on a larger sample.

The torque on an object depends on several different factors: the *shape* of the object, which determines the quadrupole moment, the external *tidal field* in which the object finds itself, and the *alignment* (or lack thereof) between the shape and the tidal field. Our results show that all of these factors are highly variable and only weakly correlated with other parameters. Thus groups of identical mass and/or binding energy can end up with very different λ values, and nearby objects may spin in very different directions.

A general inference to be drawn from these conclusions is that theories of galaxy formation in which tidally generated λ is linked to Hubble type are unlikely to produce the tight relation between local density and galactic morphology demanded by observations (Dressler 1980). The large number of nearly independent factors which combine to determine λ will produce a broad distribution of λ values in any environment. For example, the weak trend of λ and environment found in the CDM models, if coupled with the usual hypothesis that rapidly rotating protogalaxies become spirals while slow rotators become ellipticals (Sandage *et al.* 1970), would yield a broad mix of types in all settings, with spirals slightly *more* common at high densities.

If λ does not determine Hubble type, what effect does it have? It seems reasonable to suppose that galactic disks collapse until they become rotationally supported; other things being equal, disks formed from high-λ protogalaxies should have low surface densities. EB noted that the distributions of model λ values and observed surface brightnesses are consistent with this suggestion, and suggested that with sufficient photometry the relative λ values of different galaxies could be inferred by comparing surface brightness. On the other hand, the transport of angular momentum during the collapse and virialization phases of galaxy formation warns us that the specific angular momentum of a halo as a whole may not be simply related to that of the galaxy forming inside it. This effect is likely to depend critically on the spatial distribution of the gas relative to the dark matter during galaxy formation. We hypothesize that the *cooling time* of the gas within a protogalaxy could be extremely important in determining galactic morphology. If an initial protocloud is highly inhomogeneous and the cooling time is short compared to the dynamical times of the subclumps, then much of the gas could fall into separate density centers. These would then lose orbital angular momentum as they spiral toward a common center. The resulting luminous object could then resemble an elliptical galaxy or the spheroidal component of a spiral. If, however, the cooling time is much longer than the dynamical time of the dissipationless component but shorter than a Hubble time, the bulk of the gas will not collapse until most of the substructure in the halo has been erased and the background potential has become steady. These conditions seem appropriate for the formation of spiral disks. Detailed inhomogeneous and non-axisymmetric models of galaxy formation may be required to predict the gross morphology and relative specific angular momenta of the various luminous components. These ideas will be extended in subsequent investigations.

We wish to thank the other members of the DEFW collaboration: Marc Davis, Carlos Frenk, and Simon White, who have allowed us to use various N-body models. We are particularly grateful to Simon White, with whom we discussed many aspects of this paper. We also thank Nick Kaiser for useful comments. J. B. and G. E. thank the Institute of Astronomy and the Institute for Advanced Study, respectively, for providing opportunities and facilities for this collaboration. This work was supported in part by NSF grant PHY-8440263.

APPENDIX

THE CLUSTER-FINDING ALGORITHM

Clusters of particles were identified from the instantaneous particle positions, using the following algorithm:

```
For each particle p repeat
   Place p in an equivalence class by itself;
Endrepeat;
For each particle p repeat
   Find all particles {q} within x_sph of p;
   If there are n_sph or more particles {q} then
      For each q in {q} repeat
         Merge equivalence classes to which p and q belong;
      Endrepeat;
   Endif;
Endrepeat;
Output equivalence classes C of N_min or more particles.
```

Following S. White, we have used a P3M-style grid of particle lists to speed up the process of finding the set of nearby particles $\{q\}$. Techniques for representing equivalence classes are given in Knuth (1968). This algorithm depends on three parameters: $x_{\rm sph}$, $n_{\rm sph}$, and $N_{\rm min}$. The first two jointly determine a density characteristic of the clusters identified, $3n_{\rm sph}/4\pi x_{\rm sph}$, which is roughly the local density near the surface of a cluster, smoothed on a scale of $x_{\rm sph}$. The third parameter, $N_{\rm min}$, sets a floor on the size of clusters found.

REFERENCES

Bahcall, N. A., and Soneira, R. M. 1983, *Ap. J.*, **270**, 20.
Bardeen, J. M. 1986, in *Inner-Space/Outer-Space*, ed. E. W. Kolb, M. S. Turner, D. Lindley, K. Olive, and D. Seckel (Chicago: University of Chicago Press), p. 212.
Bardeen, J. M., Bond, J. R., Kaiser, N., and Szalay, A. S. 1986, *Ap. J.*, **304**, 15.
Binggeli, B. 1982, *Astr. Ap.*, **107**, 338.
Binney, J. 1974, *M.N.R.A.S.*, **168**, 73.
Binney, J., and May, A. 1986, *M.N.R.A.S.*, **218**, 743.
Binney, J., and Silk, J. 1979, *M.N.R.A.S.*, **188**, 273.
Blumenthal, G. R., Faber, S. M., Primack, J., and Rees, M. J. 1984, *Nature*, **311**, 517.
Bond, J. R., and Efstathiou, G. 1984, *Ap. J.* (*Letters*), **285**, L45.
Burstein, D., Davies, R. L., Dressler, A., Faber, S. M., Lynden-Bell, D., Terlevich, R., and Wegner, G. 1986, in *The Extragalactic Distance Scale and Deviations from the Hubble Flow*, ed. B. Madore (Dordrecht: Reidel), in press.
Collins, A., Joseph, R. D., and Robertson, N. A. 1986, *Nature*, **320**, 506.
Crampin, D. J., and Hoyle, F. 1964, *Ap. J.*, **140**, 99.
Davies, R. L., Efstathiou, G., Fall, S. M., Illingworth, G., and Schechter, P. L. 1983, *Ap. J.*, **266**, 41.
Davis, M., Efstathiou, G., Frenk, C. S., and White, S. D. M. 1985, *Ap. J.*, **292**, 371.
Davis, M., and Peebles, P. J. E. 1977, *Ap. J. Suppl.*, **34**, 425.
Dekel, A., and Silk, J. 1986, *Ap. J.*, **303**, 39.
Dekel, A., West, M. J., and Aarseth, S. J. 1984, *Ap. J.*, **279**, 1.
Doroshkevich, A. G. 1970, *Astrofizika*, **6**, 581.
Dressler, A. 1980, *Ap. J.*, **236**, 351.
Efstathiou, G., and Barnes, J. 1983, in *Proc. 3d Moriond Astrophysics Meeting, Formation and Evolution of Galaxies and Large Structures in the Universe*, ed. J. Audouze and J. Tran Thanh Van (Dordrecht: Reidel), p. 361.
Efstathiou, G., Davis, M., Frenk, C. S., and White, S. D. M. 1985, *Ap. J. Suppl.*, **57**, 241.
Efstathiou, G., and Eastwood, J. W. 1981, *M.N.R.A.S.*, **194**, 503.
Efstathiou, G., Fall, S. M., and Hogan, C. 1979, *M.N.R.A.S.*, **189**, 203.

Efstathiou, G., and Jones, B. J. T. 1979, *M.N.R.A.S.*, **186**, 133.
Faber, S. M. 1982, in *Astrophysical Cosmology: Proc. Vatican Study Week on Cosmology and Fundamental Physics*, ed. H. A. Bruck, G. V. Coyne, and M. S. Longair (Rome: Specola Vaticana), p. 219.
Fall, S. M., and Efstathiou, G. 1980, *M.N.R.A.S.*, **193**, 189.
Frenk, C. S., Davis, M., White, S. D. M., and Efstathiou, G. 1987, in preparation.
Frenk, C. S., White, S. D. M., Efstathiou, G., and Davis, M. 1985, *Nature*, **317**, 595.
Gott, J. R. 1975, *Ap. J.*, **201**, 296.
Gott, J. R., and Thuan, T. X. 1976, *Ap. J.*, **204**, 649.
———. 1978, *Ap. J.*, **223**, 425.
Gott, J. R., Turner, E. L., and Aarseth, S. J. 1979, *Ap. J.*, **234**, 485.
Gunn, J. 1982, in *Astrophysical Cosmology: Proc. Vatican Study Week on Cosmology and Fundamental Physics*, ed. H. A. Bruck, G. V. Coyne and M. S. Longair (Rome: Specola Vaticana), p. 233.
Hawley, D. L., and Peebles, P. J. E. 1975, *A.J.*, **80**, 477.
Helou, G. 1984, *Ap. J.*, **284**, 471.
Hoffmann, Y. 1986, *Ap. J.*, **301**, 65.
Hoyle, F. 1949, in *Problems of Cosmological Aerodynamics*, ed. J. M. Burgers and H. C. van de Hulst (Internat. Union Theoret. Appl. Mech. & Internat. Astr. Union), p. 195.
Kaiser, N. 1984, *Ap. J. (Letters)*, **284**, L9.
———. 1986, in *Inner-Space/Outer-Space*, ed. E. W. Kolb, M. S. Turner, D. Lindley, K. Olive, and D. Seckel (Chicago: University of Chicago Press), p. 258.
Kendall, M. G. 1975, *Multivariate Analysis* (London: Griffin).
Knuth, D. E. 1968, *The Art of Computer Programming*, Vol. **1**, *Fundamental Algorithms* (New York: Addison-Wesley).
Jones, B. J. T. 1976, *Rev. Mod. Phys.*, **48**, 107.
Lake, G. 1983, *Ap. J.*, **264**, 408.
Peebles, P. J. E. 1969, *Ap. J.*, **155**, 393.
———. 1974, *Ap. J. (Letters)*, **189**, L51.
———. 1980, *The Large-Scale Structure of the Universe* (Princeton: Princeton University Press).
———. 1981, *Ap. J.*, **248**, 885.
Quinn, P. J., Salmon, J. K., and Zurek, W. H. 1986, *Nature*, **322**, 329.
Rees, M. J. 1985, *M.N.R.A.S.*, **213**, 75P.
Rubin, V. C., Burstein, D., Ford, W. K., and Thonnard, N. 1985, *Ap. J.*, **289**, 81.
Sandage, A., Freeman, K. C., and Stokes, N. R. 1970, *Ap. J.*, **160**, 831.
Sharp, N., Lin, D. N. C., and White, S. D. M. 1979, *M.N.R.A.S.*, **187**, 287.
Silk, J. 1985, *Ap. J.*, **297**, 1.
Silk, J., and Norman, C. 1981, *Ap. J.*, **247**, 59.
Thuan, T. X., and Gott, J. R. 1977, *Ap. J.*, **216**, 194.
White, S. D. M. 1976, *M.N.R.A.S.*, **177**, 717.
———. 1984, *Ap. J.*, **286**, 38.
White, S. D. M., Frenk, C. S., Davis, M., and Efstathiou, G. 1987, *Ap. J.*, **313**, 505.
White, S. D. M., and Rees, M. J. 1978, *M.N.R.A.S.*, **183**, 341.
Zel'dovich, Ya. B. 1970, *Astr. Ap.*, **5**, 84.
Zel'dovich, Ya. B., and Novikov, I. D. 1983, in *Relativistic Astrophysics*, Vol. **2**, ed. G. Steigman (Chicago: University of Chicago Press), p. 384.

JOSHUA BARNES: Institute for Advanced Study, Princeton, NJ 08540

GEORGE EFSTATHIOU: Institute of Astronomy, Madingley Road, Cambridge CB3 0HA, UK